Anatomy of the Antarctic Circumpolar Current volume transports through Drake Passage

Zoé Koenig, Christine Provost, Young-Hyang Park, Ramiro Ferrari, Nathalie Sennéchael

To cite this version:

Zoé Koenig, Christine Provost, Young-Hyang Park, Ramiro Ferrari, Nathalie Sennéchael. Anatomy of the Antarctic Circumpolar Current volume transports through Drake Passage. Journal of Geophysical Research. Oceans, 2016, 121 (4), pp.2572-2595. 10.1002/2015JC011436 . hal-01305033

AGU PUBLICATIONS

JGR

Journal of Geophysical Research: Oceans

RESEARCH ARTICLE

10.1002/2015JC011436

Key Points:

- ACC transports in Drake Passage: energetic intraseasonal fluctuations
- Different SLA signature for barotropic and baroclinic component
- Barotropic Basin Modes in the Yaghan Basin

Correspondence to:
Z. Koenig,
zklod@locean-ipsl.upmc.fr

Citation:
Koenig, Z., C. Provost, Y.-H. Park, R. Ferrari, and N. Sennéchael (2016), Anatomy of the Antarctic Circumpolar Current volume transports through Drake Passage, *J. Geophys. Res. Oceans*, *121*, doi:10.1002/2015JC011436.

Received 3 NOV 2015
Accepted 7 MAR 2016
Accepted article online 11 MAR 2016

Anatomy of the Antarctic Circumpolar Current volume transports through Drake Passage

Zoé Koenig[1], Christine Provost[1], Young-Hyang Park[1], Ramiro Ferrari[2], and Nathalie Sennéchael[1]

[1]Laboratoire LOCEAN-IPSL, Sorbonne Universités (UPMC, Univ Paris 6)-CNRS-IRD-MNHN, Paris, France, [2]CIMA/CONICET-UBA and UMI IFAECI-3351, Buenos Aires, Argentina

Abstract The 20 year (October 1992 to August 2013) observation-based volume transport time series of the Antarctic Circumpolar Current (ACC) through Drake Passage (DP) across the Jason altimeter track #104 is analyzed to better understand the ACC transport variability and its potential causes. The time series of three transport components (total (TT), barotropic (BT), and baroclinic (BC)) referenced to 3000 m present energetic intraseasonal fluctuations, with a salient spectral peak at 50 and 36 days, with the largest (least) variance being associated with the BT (BC) component. Low-frequency variations are much less energetic with a significant variance limited to the annual and biannual timescales and show a nonstationary intermittent link with the Southern Annular Mode and the Nino 3.4 index for interannual timescales. The region around 57°S in the Yaghan Basin appears to be a strategic point for a practical monitoring of the ACC transport, as the whole-track TT is significantly correlated with the local TT ($r = 0.53$) and BT ($r = 0.69$) around 57°S. These local BT (and TT) variations are associated with a well-defined tripole pattern in altimetric sea level anomaly (SLA). There is evidence that the tripole pattern associated with BT is locally generated when the BC-associated mesoscale SLAs, which have propagated eastward from an upstream area of DP, cross the Shackleton Fracture Zone to penetrate into the Yaghan Basin. Barotropic basin modes excited within the Yaghan Basin are discussed as a plausible mechanism for the observed energy-containing intraseasonal spectral peaks found in the transport variability.

1. Introduction

The Southern Ocean is home to the largest ocean current, the Antarctic Circumpolar Current (ACC). There is no barrier to zonal flow between Cape Horn (55°S) and the Antarctic Peninsula (62°S), and the clockwise circulation of the ACC around the Antarctic continent provides a physical connection for the transport of heat, freshwater, and other tracers between the Atlantic, Indian, and Pacific Oceans. The transport and variability of the ACC are therefore of considerable importance because of their influence on climate and ecosystem processes over much of the Southern Ocean.

Many observational studies have sought to establish how the transport of the ACC varies with time and space. Most of these have focused on the flow through Drake Passage (DP), since all the transport through that section contributes to the circumpolar transport, and complications with additional flows are safely avoided. *Meredith et al*. [2011] thoroughly reviewed the past and present monitoring in DP and the major breakthroughs concerning the complex structure of the ACC and the quantification of the ACC transport in particular. The landmark International Southern Ocean Studies (ISOS) program (1974–1981) with intensive field experiments in DP (in particular the Drake 79 mooring array) provided fundamental insights into the spatial and temporal structure of the flow. The ACC flow is not spatially uniform, rather it is mostly concentrated in three main energetic fronts; from north to south: the Subantarctic Front (SAF), the Polar Front (PF) and the Southern ACC Front (SACCF) [*Nowlin et al*., 1977; *Orsi et al*., 1995] (Figure 1). From the ISOS measurements, *Whitworth* [1983] and *Whitworth and Peterson* [1985] estimated the canonical value of total ACC transport of 134 Sv (1 Sv $= 10^6$ m^3 s^{-1}) with a standard deviation of 11 Sv for a year-long record.

Whitworth and Peterson [1985] suggested that although three-quarters of the total transport is in the baroclinic component, transport variability is mainly barotropic for time scales up to around annual, allowing it to be measured by bottom pressure recorders. In contrast to this, reanalysis of the ISOS mooring data led *Cunningham et al*. [2003] to argue that the barotropic and baroclinic variability are comparable even on

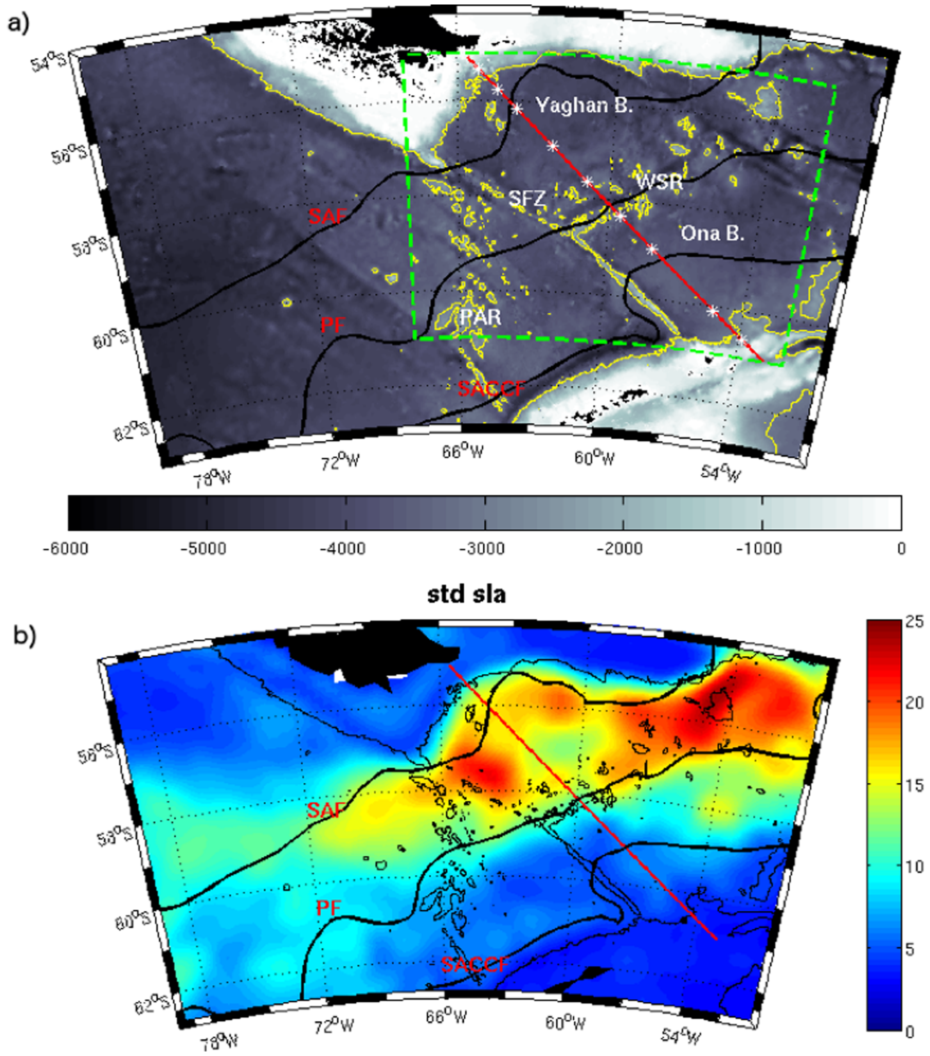

Figure 1. (a) Bathymetry in the Drake Passage in meters. Yaghan B.: Yaghan Basin; Ona B.: Ona Basin; SFZ: Shackleton Fracture Zone; WSR: West Scotia Ridge; PAR: Phoenix Antarctic Ridge. The red line is the Jason satellite altimeter ground track 104, over which the 2006–2009 current meter mooring locations (M1 through M10) are indicated. The black lines represent the climatic location of the fronts according to *Orsi et al.* [1995]. SAF: Subantarctic Front; PF: Polar Front; SACCF: Southern ACC Front. The green box is the region where the extrema are examined (see section 3). Yellow contours are the 3000 m isobath. (b) Standard deviation of the sea level anomaly in centimeter. Bathymetric contours represent the 3000 m isobath.

subseasonal timescales. Other analyses have suggested that barotropic variability dominates the transport through DP on time scales up to seasonal, with baroclinic variability becoming important at annual and interannual timescales [*Hughes et al*, 2003; *Meredith et al.*, 2004]. However, the interannual variations of the ACC transport appear to be rather small [*Meredith et al.*, 2011], despite a significant positive trend in the Southern Annular Mode (SAM) index seen in recent decades [*Thompson and Solomon*, 2002]. A hypothetic explanation is that the ACC becomes “eddy saturated” with excess energy from the stronger winds being cascaded to mesoscale length scales via baroclinic instability [*Hallberg and Gnanadesikan*, 2006; *Meredith and Hogg*, 2006]. This remains to be verified with long-term observational data.

The satellite altimetry era started in 1992 and opened new perspectives to the monitoring of the ACC circulation and its transport variability through DP. For example, *Barré et al.* [2011] monitored precise frontal locations and identified recurrent flow patterns in DP. To achieve the objective of transport monitoring using altimetry, hydrographic data and current meter time series were collected during 3 years (2006–2009) along the ground track 104 of Jason altimeter satellite as part of the DRAKE project [*Provost et al.*, 2011]. The in situ data were located parallel and downstream of the Shackleton Fracture Zone (SFZ), running through the Yaghan Basin north of the West Scotia Ridge (WSR) and the Ona Basin south of the WSR (Figure 1), two semiclosed basins below 3000 m

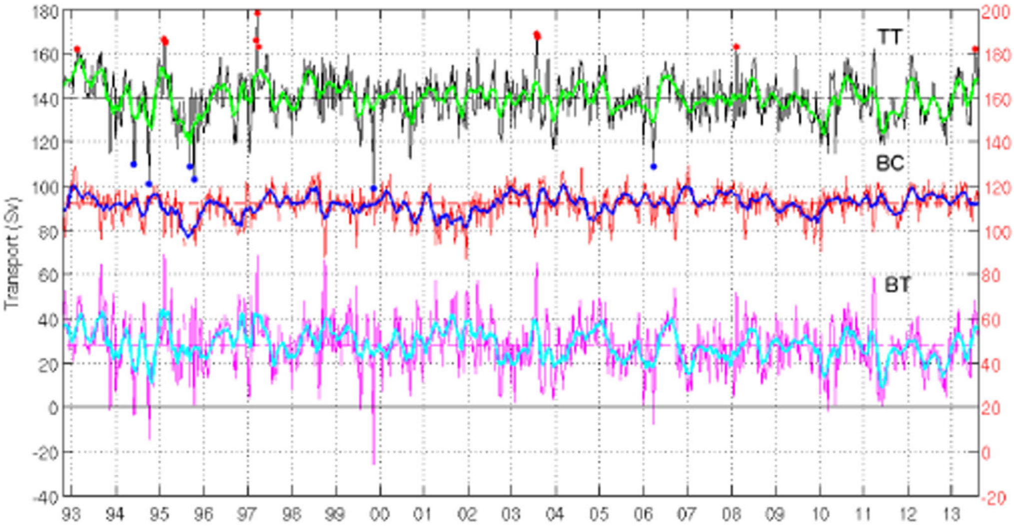

Figure 2. Time series of the total (black), baroclinic (red), and barotropic (magenta) transport referenced to 3000 m, with superimposed smoothed series obtained using a 1 month running mean. Total transport (mean ± std): 140 ± 10 Sv; barotropic transport: 28 ± 13 Sv; baroclinic transport: 112 ± 7 Sv. The red axis on the right refers to the baroclinic transport. The red dots are the total transport greater than 162 Sv and the blue dots smaller than 110 Sv.

(Figure 1). The Drake in situ data have been used to evaluate the altimetry products. Both hydrographic data with lowered acoustic Doppler current profiler (LADCP) transects and moored velocity time series showed that altimetric data, and in particular the multisatellite gridded products provided accurate information on surface geostrophic velocity variations [*Barré et al*., 2011; *Ferrari et al*., 2012, 2013].

A 20 year (October 1992 to August 2013) ACC transport time series referenced to 3000 m with a 7 day resolution has been produced from the combination of information from 3 years of in situ velocity data (2006–2009) and satellite altimetric observations of surface currents along the Jason ground track #104 (from the multisatellite-gridded product interpolated to the Jason track #104) [*Koenig et al*., 2014]. Note that the Yaghan Basin and the Ona Basin are almost closed below 3000 m, such that the net transport below 3000 m is almost zero, compensating cross-track transports along the track [see *Koenig et al*., 2014 for more details]. We produced time and space-varying transfer functions (or the look-up table) relating altimetry-derived surface currents to velocity profiles in the water column derived from the 2006–2009 current-meter mooring data. The transport time series was then extended over the altimetric era with a time resolution of 7 days. This time series was decomposed into three transport components: total transport (TT), baroclinic transport (BC), and the barotropic transport (BT) (Figure 2). The baroclinic transport is calculated relative to a zero velocity at 3000 m and the barotropic transport is calculated by integrating the velocity at 3000 m (or the bottom if shallower) over the upper 3000 m of the water column.

This paper analyzes the variations observed in the above three transport time series (total, baroclinic, and barotropic transports referenced to 3000 m) and examines the potential dynamical drivers of the observed variations. The following scientific questions are addressed: Are the time series stationary? What are their respective spectral contents? How do baroclinic and barotropic components vary in space and time, and how do they contribute to the total transport variability at DP? What are the large-scale atmospheric forcings responsible for the low-frequency variations?

The paper is organized as follows. Section 2 describes the three volume transport time series (TT, BT, and BC) and provides a spectral analysis. The time series are nonstationary and the evolution of their spectral content and coherences are carefully examined. Section 3 considers the along-track distribution of the three transport components. It presents an empirical orthogonal function (EOF) analysis of the along-track variations in the three transports, a study of the along-track relationship between BT and BC and a description of synoptic situations corresponding to the extrema of TT. Section 4 examines statistical relationships between variations in the three transports and regional sea level at different lags. Section 5 investigates potential drivers of the variations in the transport time series. Section 6 summarizes and discusses the results.

2. Statistics and Spectral Content of Transport Time Series

2.1. Transport Uncertainty

Table 1. Mean, Standard Deviation (std), Standard Error of the Mean (sem), and Range of the Total (TT), Barotropic (BT), and Baroclinic (BC) for the Raw Transports (Left) and the Smoothed Transports (Right) With a 1 Month Running Mean

	Raw Transport			Smoothed Transport		
	TT	BC	BT	TT	BC	BT
Mean	140	112	28	140	112	28
Std	10	7	12	7.6	4.1	6.5
Sem	2.2	1.6	1.6	1.6	1.6	1.6
Range	79	42	95	38	24	36

The volume transport was reconstructed using a look-up table (established from the current-meter data at nine moorings) and the surface velocities (gridded satellite altimetric data with a 7 day and 1/4° resolution) [see *Koenig et al.*, 2014 for more details]. Therefore small-scale variations in transport between coarsely spaced (~50–80 km) current-meter mooring lines are projected from the finer-resolution altimetric data (~25 km) via the look-up table constructed from the current meter data. Several comparisons have been done in *Koenig et al.* [2014] to estimate the uncertainties on the BC and TT components.

Current meter moorings used to elaborate the look-up table were not closely spaced and did not carry instruments below 3000 m. However, we compared with two high-resolution cross-track geostrophic velocity sections derived from CTD data referenced to LADCP data [*Renault et al.*, 2011]. The two sections were performed within 3 weeks and have a horizontal resolution of 20 km between stations, close to the altimetric data resolution, and a vertical resolution of 10 m, similar to the look-up table. These two sections as well as four sections of reconstructed velocities obtained using altimetry and the lookup table are shown in *Koenig et al.* [2014] (their Figure 9). The reconstructed velocity transects and corresponding total transports are in good agreement with those derived from the in situ data, which is remarkable considering the difference in time resolution (in situ sections performed in 7 to 10 days) and the rapid evolution of the flow [*Barré et al.*, 2011]. The differences in TT, BC, and BT referenced to 3000 m between the reconstructed and observed transports are 4, 2, and 7 Sv, respectively.

The internal consistency and the robustness of the method to estimate the TT transport were carefully assessed in *Koenig et al.* [2014]. Sensitivity studies were performed using model outputs to evaluate uncertainties due to mooring spacing [*Koenig et al.*, 2014] (subsection 6.4). We also compared the two methods "look-up table" and "classical" to compute the volume transport [*Koenig et al.*, 2014, Appendix B]. These sensitivity studies led us to assess that the uncertainties on the 7 day resolution TT are around 7 Sv [*Koenig et al.*, 2014]. The uncertainty on the 5 week-smoothed TT is smaller (3.6 Sv when comparing the two methods) [*Koenig et al.*, 2014; Appendix B].

The accuracy of the BC transport was also assessed in *Koenig et al.* [2014] and the uncertainties estimated around 7 Sv by comparing the reconstructed weekly BC transports and the transports obtained from historical hydrographic sections [see *Koenig et al.*, 2014 their Figure 15, section 6.1]. It is more difficult to assess precise errors on the BT. We estimate that the uncertainty on the weekly BT is comparable to the one on the BC (7 Sv).

2.2. Basic Statistics

The time series of the three transport components referenced to 3000 m are shown in Figure 2 and their basic statistics are given in Table 1. The mean net transport across the track over 20 years (October 1992 to August 2013) is 140 Sv. The mean baroclinic transport is overwhelming (112 Sv or 80% of TT), with a small contribution from the mean barotropic transport (28 Sv or 20% of TT). Marginally significant trends (at the 95% confidence level) are observed in the transport time series: a small decrease in total volume transport (-4.3 ± 2.1 Sv in 20 years), a larger decrease in barotropic transport (-7 ± 2.4 Sv in 20 years) and a small increase in baroclinic transport ($+2.7 \pm 1.3$ Sv in 20 years) [*Koenig et al.*, 2014].

The barotropic transport exhibits a large variability with a standard deviation (std) of 12 Sv, which can be compared with significantly smaller variability for BC (7 Sv) and TT (10 Sv). The TT variability is smaller than that of BT because the BT and BC time series are anticorrelated at -0.5, significant at the 99% confidence level.

Drake Passage weekly transports during the past two decades vary over wide ranges: 79 Sv (from 99 to 178 Sv) for TT, 42 Sv (from 87 to 129 Sv) for BC, and 95 Sv (from -26 to 69 Sv) for BT. Short-term variations present

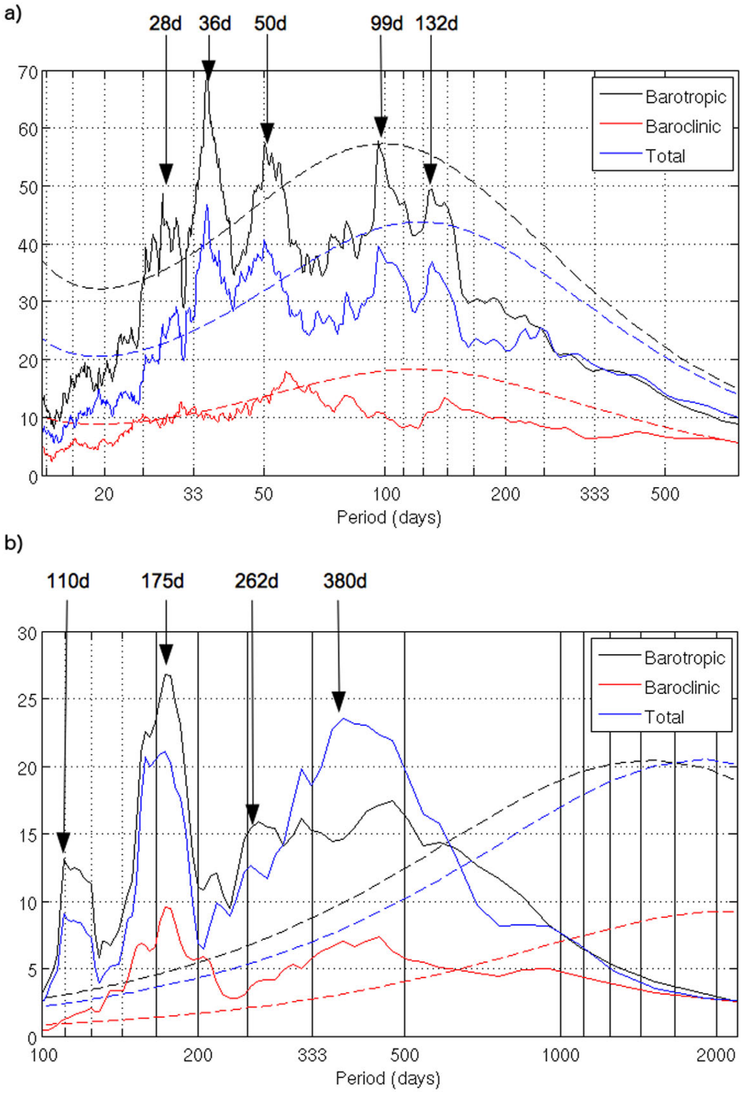

Figure 3. Variance-preserving spectra of (a) the full-time resolution transport time series (TT, BC, and BT) (by averaging over groups of 31 adjacent frequencies) and (b) the monthly smoothed transport time series (by averaging over groups of 11 adjacent frequencies). The dotted lines show the 95% confidence level against the red noise background from a first order autoregressive (AR1) process. The *y* axis is the power in Sv^2.

throughout the three transport time series have large amplitudes (Figure 2), which can vary by more than 25 Sv in less than 3 weeks, as already reported in by *Koenig et al.* [2014]. Monthly low-pass-filtered time series (with a 5 week running mean) have reduced but still significant variability, with a comparable std (range) for the three time series: 7.6 (38) Sv for TT, 4.1 (24) Sv for BC, and 6.5 (36) Sv for BT.

2.3. Spectral Content of the Transport Components

All transport time series are dominated by high-frequency variations (Figure 2). The first zero crossing of the autocorrelation function yields an integral time scale of 19 days for TT, 31 days for BC, and 11 days for BT, giving a large number of degrees of freedom (200 for TT, 350 for BT, and 120 for BC) for the 20 year long time series. These are used for the calculation of a significant level.

The energy-conserving spectra emphasizing intraseasonal variations of periods shorter than 5 months are presented by averaging over groups of 31 adjacent frequencies (Figure 3a). Here, the most energetic variations are found in BT (max 69 Sv^2), which are significantly greater than those in TT (max 47 Sv^2) or BC (max 18 Sv^2). Several salient bands of elevated energy (significant at the 95% confidence level) are observed for both BT and TT, with significant peaks centered at 50, 36, and 28 days. Although not significant at the 95% level distinctive energy-containing bands centered at 99 and 132 days for the above two transport components are observed. Of these, the outstanding peak centered at 50 days is commonly observed for all three components of transport (with a slight frequency shift in the baroclinic transport with the maximum energy at 57 days), which we interpret as the representative period of the intraseasonal transport variability in DP. The 50 day peak in the baroclinic transport is consistent with *Chidichimo et al.* [2014].

In order to study the low-frequency variability using the monthly smoothed transport time series, the energy-conserving spectra for periods greater than 4 months are presented by averaging 11 nearby frequencies (Figure 3b). Energy levels drop considerably for periods greater than 4 months in which the spectral energy rarely exceeds 25 Sv^2. Although much weaker than the intraseasonal variability, there appears a spectral bump in the seasonal timescale around the semiannual period (175 days). For the interannual timescale, the three transport time series have a significant energy peak between the annual and biannual periods but insignificant variability for periods greater than 2 years.

The time series are not stationary, but rather their spectral contents evolve with time. A wavelet analysis of the monthly time series smoothed with a 1 month running mean (not shown) shows that significant energy near the semiannual period is omnipresent in all three time series, except for BT from 2005 to 2010 during which significant energy is found for somewhat longer periods (centered around 9 months). The variability associated with BT has much less energy at the annual to biannual periods compared to high frequencies, and significant energy is only found from 1994 to 1999 and during the second half of the time series after 2002. Although not significant, the 5 year variability is most energetic for BC compared to BT and TT especially during the first half of the time series until 2003, while no comparable variability is associated with BT.

2.4. Coherence Among the Transport Components (Unsmoothed 7 Day Resolution)

Koenig et al. [2014] have shown that the BT and BC time series present a high degree of anticorrelation (-0.5). The wavelet coherence analysis shows that the anticorrelation between BT and BC is present at all periodicities (although significantly weaker around the 1-year period) (Figure 4a). The intermittent large anticorrelation may suggest an occasional strong link between the barotropic and baroclinic components which will be examined in detail in section 3.

The partition of the total transport into its barotropic and baroclinic components is examined through a wavelet coherence analysis (Figures 4b and 4c). Most TT variations of periods shorter than 1 year are significantly correlated with those of BT (Figure 4c), except for the 6 month period that is only episodically correlated, with no significant coherence between years 2000 and 2008. In most frequencies except for annual and 4 year periods, BC and TT are not well correlated. The annual TT variations are significantly correlated with those of BC in the first part of the time series until 2001, but this correlation disappears completely from 2002 onward (Figure 4b). This is due to a change in the relative amplitude of BT annual variations (wavelet analysis not shown). Biannual TT variations are systematically correlated with those of BT (Figure 4c). In contrast, no significant coherent variability is observed between BC and TT for the biannual timescale (Figure 4b). As a result, the total transport has a high time-mean correlation of 0.83 with the barotropic component at zero lag but only a marginal correlation of 0.22 (though still significant at the 95% confidence level) with the baroclinic component lagging by 2 weeks.

3. Along-Track Distribution of the Transport Components Referenced to 3000 m

We examine the along-track distribution of the three 7 day-resolution transport components (TT, BC, BT referenced to 3000 m) previously prepared by *Koenig et al*. [2014] who calculated the transport over regular intervals of 5.8 km along the 934 km long altimetric track. We used here the point-wise transport (in Sv) corresponding to the across-track transport per unit along-track distance of 5.8 km.

Uncertainties in transport components on each 5.8 km intervals cannot be precisely estimated away from moorings. Reconstructed cross-track velocities at the current-meter locations were compared to in situ cross-track velocities at each current-meter in *Koenig et al*. [2014] (their table 3). Differences between reconstructed and in situ velocities were similar at all moorings, although slightly larger at M3 and increased with depth. Largest uncertainties are thus expected for the BT. Uncertainty on the reconstructed BT at mooring sites (over a 5.8 km along-track distance interval) varied from 0.4 Sv at M6 to 1.3 Sv at M3. On a monthly mean, the uncertainties on the reconstructed BT at mooring sites dropped to 0.2 Sv at M6 to 1 Sv at M3.

3.1. Mean Distribution and Standard Deviation of the Transports

The three main ACC fronts are easily identified in the along-track profile of the mean total transport: the SAF around 55.75°S, the combined PF and SACCF-N between 57.75 and 58.5°S, and the SACCF-S at 60.5°S (Figure 5a, thick black line). The negative transports centered at 56.9°S in the Yaghan Basin and at 59.7°S in the Ona Basin correspond at depth to the cyclonic recirculation features described in *Ferrari et al*. [2012, 2013] and *Barré et al*. [2008], coinciding in surface with cyclonic eddies. The along-track mean transport variability (std) is 1.2 Sv, varying from 0.3 Sv at 60.7°S to a maximum of 2 Sv at 56.9°S. The transport variability is relatively large at all latitudes, without any clear distinction between the Ona and Yaghan Basins, except for the largest variability near 57°S which exceeds the along-track mean variability by a factor of almost 2.

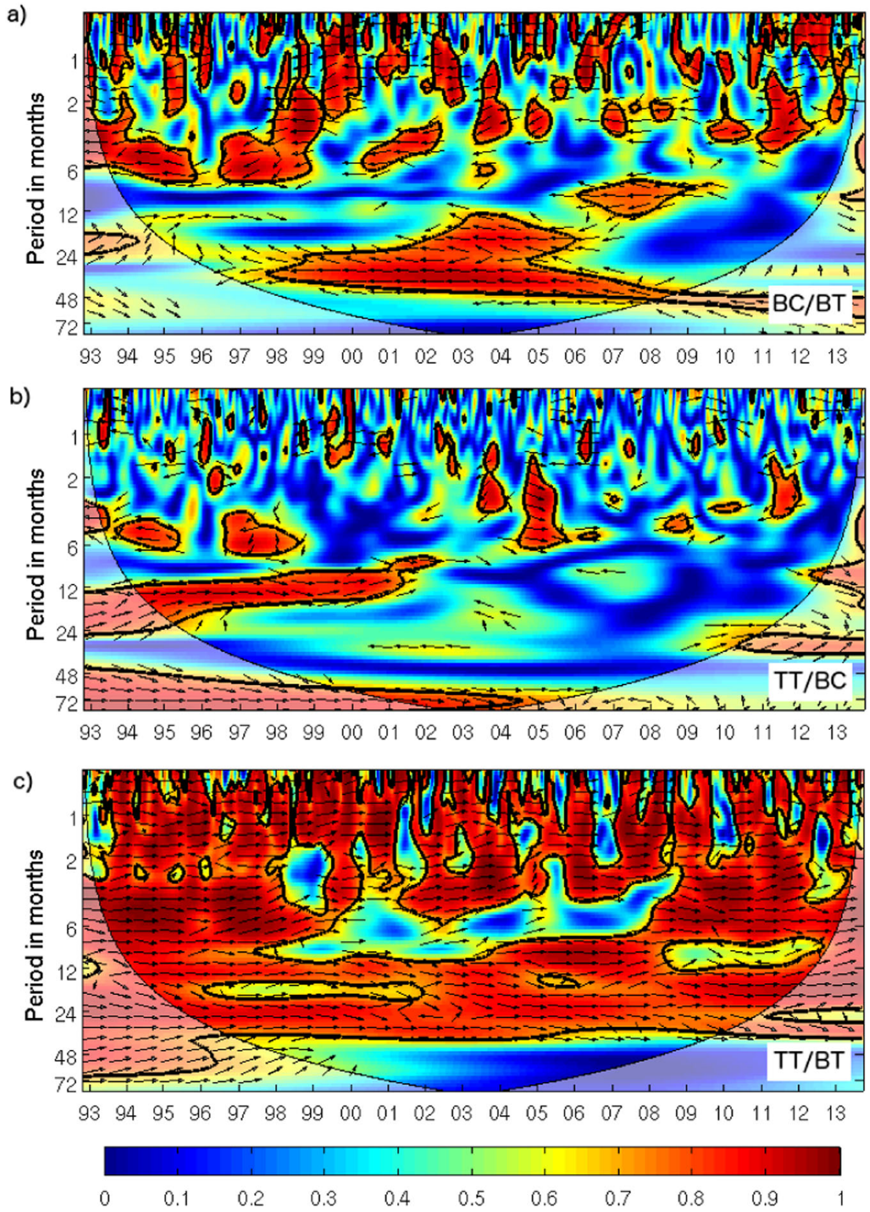

Figure 4. Wavelet coherence between different pairs of transport time series. (a) Baroclinic versus barotropic transport. (b) Baroclinic versus total transport. (c) Barotropic versus total transport. The correlation is shown in color and the phase lag in arrows turning clockwise from due east (zero lag). The black lines indicate the 95% confidence level.

The mean baroclinic transport is nearly entirely confined in the Yaghan Basin, with a negligible contribution from the Ona Basin (Figure 5b, black thick line). The SAF is clearly separated from the other fronts by an area of near zero baroclinic transport around 56.5°S. The PF and the SACCF-N are indistinguishable, with the mean baroclinic transport remaining relatively homogeneous between 0.8 and 1.4 Sv in the area between 57°S and 58.5°S. The largest baroclinic transport of 1.1 Sv in the northernmost Ona Basin is associated with the southern limb of the SACCF-N which is tightly attached to the southern slope of the WSR. In contrast, the SACCF-S located at the foot of the Antarctic continental rise in the southernmost Ona Basin peaks only at 0.4 Sv. As seen by its standard deviation amplitudes, the baroclinic transport variability is nearly entirely concentrated in the Yaghan Basin (Figure 5b).

The mean barotropic transport shows a large positive transport at 56.2°S, about 0.5° south of the mean position of the SAF (55.75°S), and a large negative transport around 56.9°S (Figure 5c, black thick line), thus forming a well-defined cyclonic recirculation pattern in the Yaghan Basin. In the Ona Basin, the barotropic

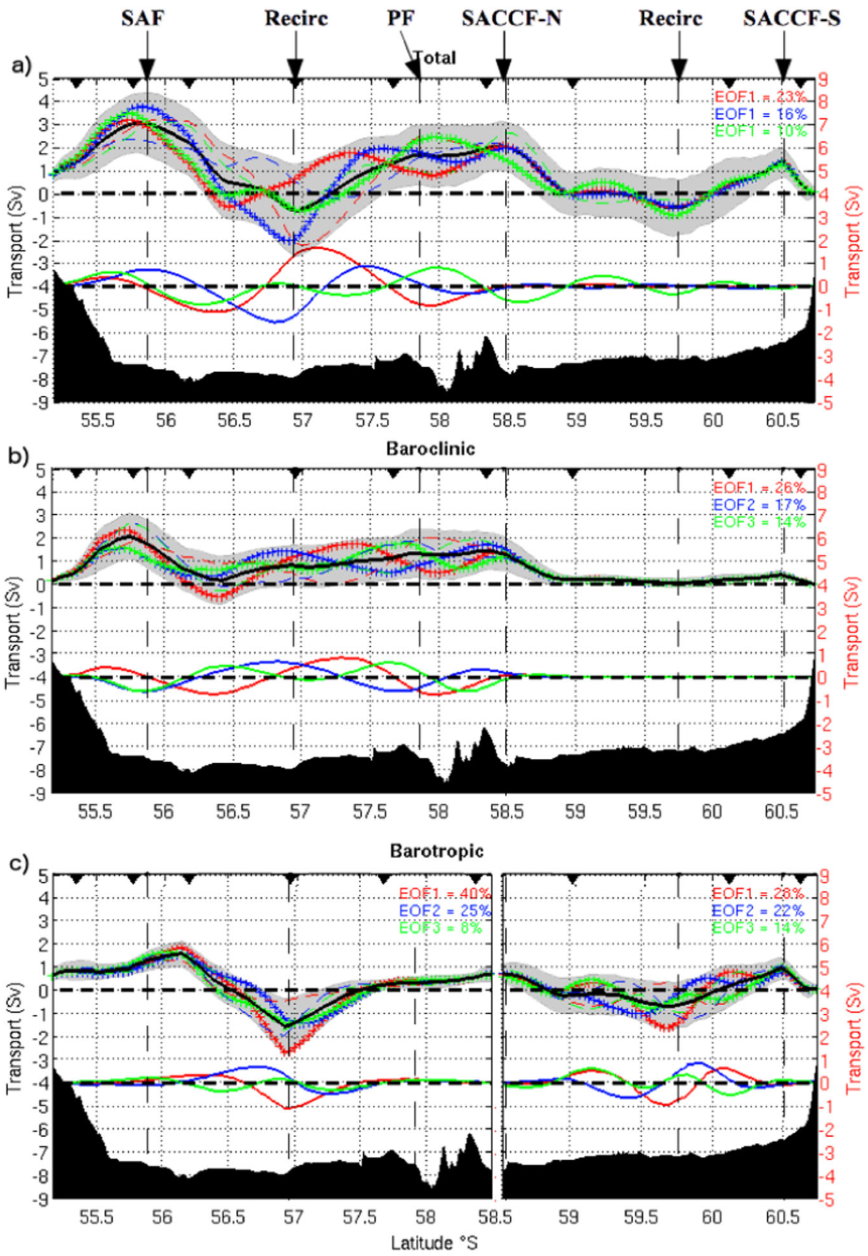

Figure 5. Empirical orthogonal function (EOF) decomposition of the (a) total, (b) baroclinic, and (c) barotropic transports along the Jason track 104. The transport is in Sv per 5.8 km. The thick black line is the mean transport and the grey shading represents the std. The three gravest EOFs corresponding to each transport component are shown below the mean transport lines and the dashed (plus-sign) lines are the mean plus (minus) the EOF. Bathymetry is shown at the bottom of each plot. The black triangles are the mooring locations.

transport represents the main component of the total transport, with negative values in the central basin centered at 59.7°S and positive values at both sides of the basin at 58.5°S (SACCF-N) and 60.5°S (SACCF-S). The barotropic transport variability at 57°S is comparable in amplitude (around 2 Sv) to that of the baroclinic transport, although the BT variability is slightly larger.

As the largest transport variability is observed at 56.9°S in the Yaghan Basin for all three transport components, the correlations between the whole-track transports and the local transports around 57°S (56.75°S–57.25°S) are computed. The correlation is strong both for BT ($r = 0.69$) and TT ($r = 0.53$), both significant at the 99% level. In contrast, a weak anticorrelation ($r = -0.34$) is observed for BC, as the BC variability is much more homogeneously distributed along the track in the Yaghan Basin (Figure 5b). Therefore, the location

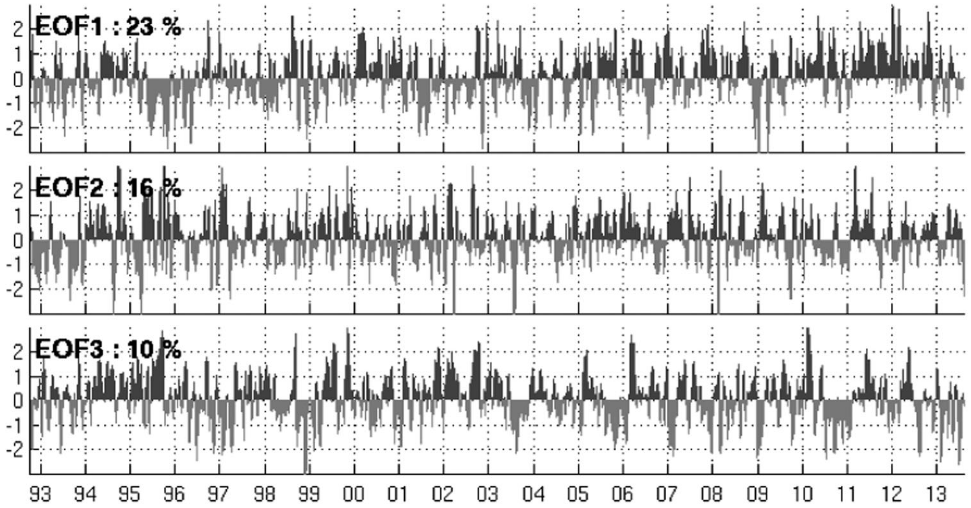

Figure 6. Principal components of the total transport time series.

around 57°S appears as a strategic point in monitoring the first order transport variability of the BT and TT across the whole track.

The 57°S latitude happens to correspond to the mooring location M4 but this does not imply a bias in the volume transport quantification. In fact, our methodology using fine-resolution (1/4°) altimetry is able to reproduce maxima at other locations than the mooring locations. For example, the region around 59.7°S in the Ona Basin reveals a local minimum in transport and its variability (see Figure 5), although no mooring was located there: the closest mooring site M9 was located around 30 km south of the transport maximum.

3.2. Along-Track Modal Variability of Transport

An empirical orthogonal function (EOF) analysis is performed to investigate along-track variations in the transport components. The first three EOFs (EOF1, EOF2, and EOF3) of each transport component are shown underneath the mean transport profiles in Figure 5, which feature well-organized wave-like spatial structures associated with rather high frequency variations of time scales varying from 3 weeks to 2 months (Figure 6). In order to better understand the contribution of each mode to the transport variability, the individual EOF is added (plus-sign line) to or subtracted (dashed line) from the mean transport profiles (bold black lines) in Figure 5.

The first two EOFs of TT (mutually independent according to North's significance test) [*North et al*., 1982], which are unique features in the Yaghan Basin and almost identically zero south of 58.5°S in the Ona Basin, reveal the largest amplitudes around 57°S. They are in quadrature and feature northward/southward shifts of the SAF and PF, yielding a negative mean transport around 57.5°S. In the EOF3, which covers the whole track, the SAF shifts northward when the PF shifts southward and vice versa. The latter mode also presents some signal in the north of the Ona Basin in particular modifying the SACCF-N amplitude and location, while the SACCF-S remains unchanged. Note that the positive phase of the TT EOF1 (the negative phase of the TT EOF2) correspond to a transport increase of 2.5 (5) Sv, with an increase of 24 (14) Sv in the area around 57°S, and a decrease of 12 (7) Sv and 10 (2) Sv in the SAF and PF area, respectively. Thus the increase in the total transport is mainly due to an increase in the transport around 57°S.

The baroclinic transport component reveals its greatest EOF modes (mutually independent according to North's significance test) [*North et al*., 1982] entirely confined in the Yaghan Basin, with no signals in the Ona Basin (Figure 5b). The EOF1 and EOF2 are of nearly same amplitude and in quadrature, indicative of propagating wave-like features across the entire Yaghan Basin. They show changing amplitude and location of the frontal system in the latter basin. In particular, the EOF1 of BC can feature negative values between 56.2 and 56.6°S, midway between the SAF and 57°S. The EOF2 modulates most significantly the transport intensity at the SAF (55.75°S) and at 57°S, but in opposite directions between the two sites.

Table 2. Correlations Between the Baroclinic/Barotropic Component in Different Part of the Yaghan Basin[a]

	SAF − BC (Std 12 Sv)	R − BC (Std 14 Sv)	PF − BC (Std 12 Sv)
SAF − BT (Std 6 Sv)	0.78	−0.64	(0.12)
R − BT (Std 14 Sv)	−0.71	0.94	−0.66
PF − BT (Std 4 Sv)	(0.15)	−0.50	0.69

[a] SAF: transport from 55°S to 56.5°S. R: transport from 56.5°S to 57.5°S. PF: transport from 57.5°S to 58.75°S. BC: baroclinic transport. BT: barotropic transport. In brackets: non significant correlations.

In contrast to the baroclinic component, the gravest EOFs of the barotropic transport are concentrated in the central part of both the Yaghan and Ona Basins (Figure 5c). It is to be noted that when the whole track is considered, the first three EOFs are not independent and explain only a small percentage of the total variance. This suggests that the BT variability in the Ona and Yaghan Basins are independent. Therefore, the EOFs shown in Figure 5c have been calculated separately in each basin, yielding the independent EOFs explaining a large amount of the total variance in each basin. In particular, the EOF1 in the Yaghan Basin, which explains 40% of the total variance, shows an original triangular-shape monopole structure with its summit coinciding with the strongest mean westward transport at 56.9°S. It clearly explains the changing intensity of the transport at 57°S, thus affecting significantly the total transport variability that is strongly concentrated around 57°S (compare Figures 5c and 5a).

The time series or principal components associated with the first three EOFs of the transport components have most of their energy at high frequencies (periods less than 2 months). An example is shown in Figure 6 for the total transport. These high frequencies are in stark contrast with the well-organized spatial patterns of the EOFs showing a representative scale of ~100km. As the baroclinic and barotropic components of transport show a significant anticorrelation ($r = -0.5$), as already mentioned, we examine below the relationship between the BC and BT components.

3.3. Along-Track Relationship Between the Barotropic and Baroclinic Transports

As the baroclinic variability in the Ona Basin is negligible, we focus on the Yaghan Basin. Time series of BT and BC transports are prepared for three subregions of the Yaghan Basin based on the climatological frontal locations (Figure 5): the SAF region from 55°S to 56.5°S (SAF-BT and SAF-BC), the center of the Yaghan Basin with a negative transport from 56.5°S to 57.5°S (R-BT and R-BC), and the PF-SACCF-N region from 57.5°S to 58.75°S (PF-BT and PF-BC). Correlations between the BT and BC transports for different pairs of subregions are given in Table 2. In each subregion, the BT and BC transports are significantly and positively correlated (see the diagonal of Table 2), indicating that at any location in the Yaghan Basin, the BT and BC components tend to covary in the same direction. This in-phase correlation is particularly large in the center region ($r \sim 0.9$), indicative of the quasi-equivalent barotropic structure of the flow in the Yaghan Basin especially around 57°S [*Ferrari et al.*, 2012].

Large anticorrelations are observed between the barotropic transport in the center region around 57°S and the baroclinic transport of both the SAF ($r = -0.71$ between R-BT and SAF-BC) and the PF ($r = -0.66$ between R-BT and PF-BC), both significant at the 99% level. This strongly suggests some seesaw-like interactions between the barotropic flow in the central part and the baroclinic flow in the northern and southern parts of the Yaghan Basin, which resembles a basin mode-like modulation.

Hence, although BC and BT covary at the same location to a degree reflecting the quasi-equivalent barotropic character of the flow, they show large anticorrelations at the scale of the Yaghan Basin, indicative of energy conversion between BC and BT. These exchanges are further examined at a basin scale in section 4.

3.4. Extrema of the Transport Time Series

We examine the along-track and basin-wide patterns associated with the extreme values of transport, based on the criteria of total transports smaller than 110 Sv or larger than 162 Sv. The total transport is smaller than 110 Sv on seven 1 week periods in 20 years (Figure 2 and Table 3). The transports in the Ona Basin bear no tight relationship with the minima. In contrast, the synoptic total transport in the Yaghan Basin during minimal total transports is much smaller (by 29 Sv) than the 20 year mean (90 versus 119 Sv). This is associated with a significant decrease (by 29 Sv) of the barotropic transport (−4 versus 25 Sv for the 20 year mean) and no change in the baroclinic transport in the Ona Basin (94 Sv).

Table 3. Statistics of Transports Over the 20 Year Long Time Series.[a]

Total			Barotropic			Baroclinic		
All	Yaghan	Ona	All	Yaghan	Ona	All	Yaghan	Ona
				Total				
140	**119**	**21**	**28**	**25**	**3**	**112**	**94**	**18**
				Maxima				
162	126	36	46	29	17	116	97	19
166	137	29	69	58	11	97	79	18
165	145	20	66	67	−1	99	79	20
166	113	53	54	26	28	112	87	25
178	132	46	68	52	16	110	81	29
163	130	33	53	50	3	110	79	31
169	138	31	65	51	14	104	87	17
167	129	38	60	48	12	107	82	25
163	161	2	52	63	−11	111	99	12
162	122	40	48	33	15	114	90	24
166	**134**	**32**	**58**	**48**	**10**	**108**	**86**	**22**
				Minima				
110	109	1	−4	12	−16	113	97	16
101	76	25	−11	−14	3	112	90	22
101	78	23	−15	−14	−1	116	92	24
109	98	11	9	12	−3	100	86	14
103	82	21	1	2	−1	102	81	21
99	86	13	−26	−25	−1	125	110	15
109	99	10	−8	−2	−6	116	101	15
105	**90**	**15**	**−7**	**−4**	**−3**	**112**	**94**	**18**

[a] Values of the transport (in Sv) corresponding to the mean over the 20 years (top), the maxima (TT>162 Sv) (middle), the minima (TT<110 Sv) (bottom). DP: transport integrated along the entire track. Yaghan: transport north of 58.5°S. Ona: transport south of 58.5°S. In bold: the mean transport.

The seven minima reveal pronounced negative transports around 57°S (Figure 7a). Both the baroclinic and barotropic transports also show large negative transports near 57°S (not shown). The minima of the total transport are associated with a pair of strong cyclonic and anticyclonic circulation patterns between the SAF and the PF, as can be seen in the altimetric surface dynamic topography corresponding to the dates of two of these minima (Figures 7e and 7f). The maps show either an "Omega" pattern with a meander to the north (Figure 7f) or a "Rex" pattern, i.e., a dipolar structure with low dynamic topography to the north and high one to the south (Figure 7e). These "Omega" and "Rex" patterns remind of the blocking patterns in the atmosphere [*Barriopedro et al*., 2010]. A « knot », here a strong cyclonic circulation, is located to the north of 57°S and extends all the way to the coast, thus decreasing the corresponding transport. The minima in TT never last more than 2 weeks (see Figure 2), however, the "knot" associated with the TT minima can be followed for 1 to 2 months in the Yaghan Basin as it moves eastward (not shown) before it falls apart.

Total transport values larger than 162 Sv occur on ten 1 week periods in 20 years (Table 3). Maxima correspond to a spatial pattern where the SAF is further south than climatology on and upstream of track #104, while the PF is further north on track #104 (Figures 7g and 7h). The average total transport of the ten maxima is 15 Sv larger than the climatology in the Yaghan Basin, while it is only 11 Sv larger in the Ona Basin (Table 3). The barotropic transport of the ten maxima (Figure 7d) is on average 29 Sv larger in the Yaghan Basin and only 6 Sv larger in the Ona Basin. In contrast to this, the baroclinc transport (not shown) across the entire track is 4 Sv smaller than the climatology. Hence, the barotropic component (mainly around 57°S) appears as the key factor for regulating the large positive/negative transport anomalies in the entire Yaghan Basin.

In summary, the extrema in TT are linked to the northward/southward meandering of the SAF in the Yaghan Basin as well as to the presence/absence of a cyclonic eddy/deep recirculation north of 57°S. As seen in section 3.1, the BT and TT transports across the whole track are highly correlated with the local transport at 57°S, which is also verified with the transport extrema.

4. Transport Variations and Sea Level Anomalies

To investigate basin-wide spatial structures associated with transport variations, we consider statistical relationships between transport variations and sea level anomalies in and around DP. The SLA field is regressed

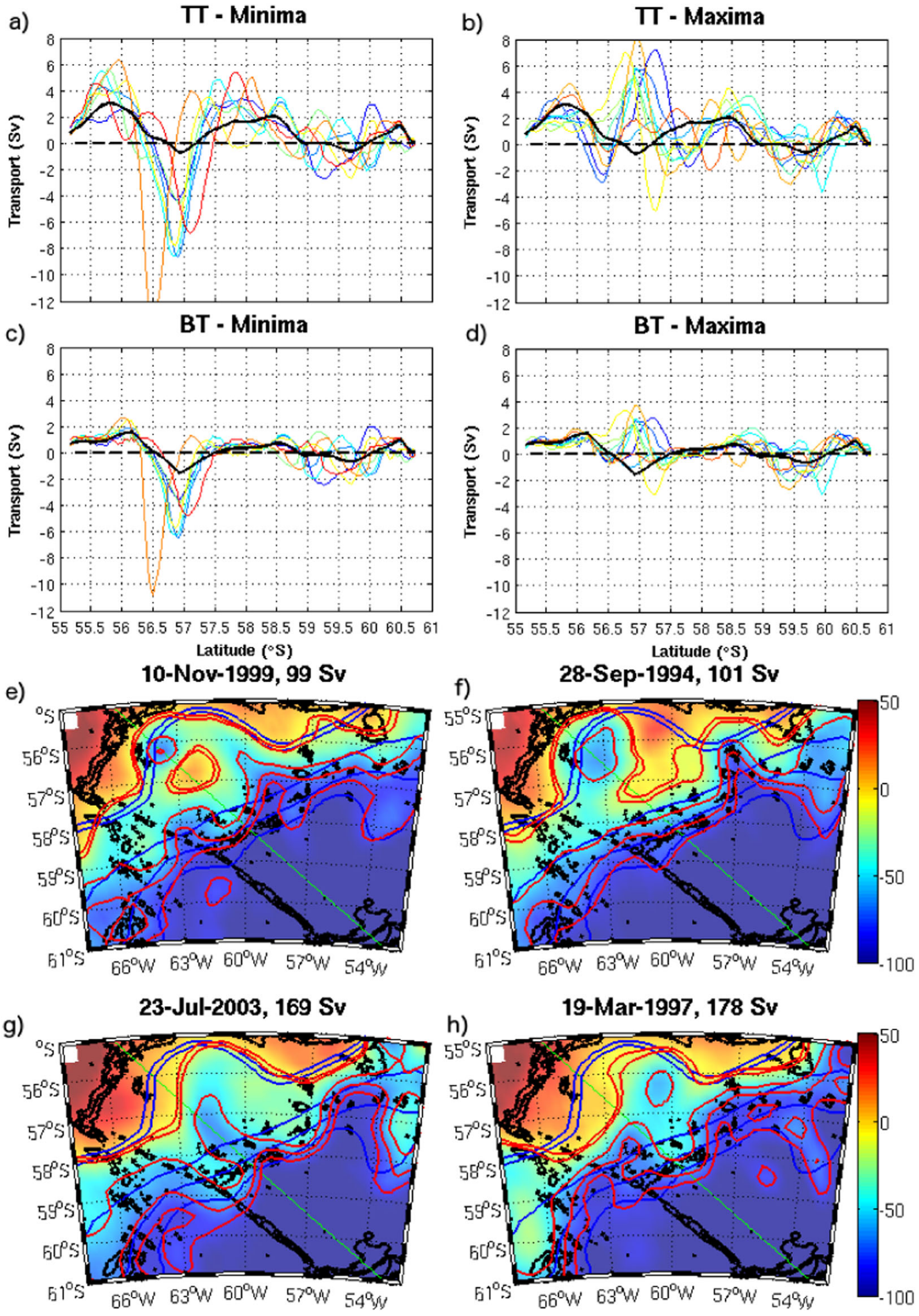

Figure 7. Along-track distribution of the total (barotropic) transport corresponding to (a) and (c) seven transport minima and (b) and (d) ten transport maxima. (e) and (f) Snapshots of absolute dynamic topography corresponding to instances of total transport less than 110 Sv. (g) and (h) Same as (e) and (f) but for the total transport greater than 162 Sv. Color scale is in centimeter. The red lines are the actual position of the fronts (two branches of the SAF, two branches of the PF and SACCF-N). The blue lines indicate the time and position of the fronts over 20 years of altimetric data. The frontal positions correspond to specific dynamic height contours; red: at the dates of the transport extrema; blue: time-mean dynamic height contours. Bathymetry is shown in bold black lines. The green line is the Jason track #104.

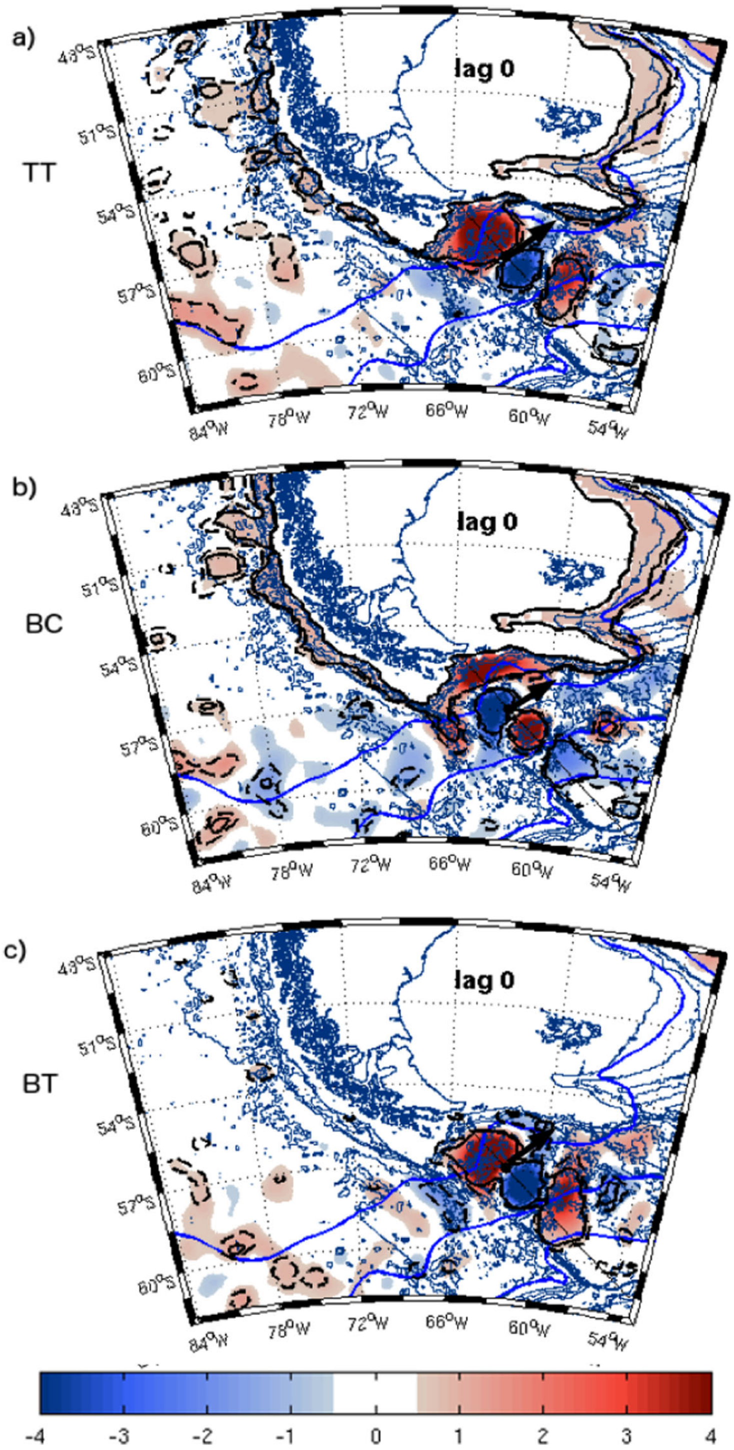

Figure 8. Regression maps of the detrended normalized transport onto the detrended SLA for (a) TT, (b) BC, and (c) TT. The color scale is in centimeter. The background faint lines represent the bathymetry. The thick (dashed) black lines are the 99 (95)% confidence level. The blue lines are the climatological fronts from *Orsi et al.* [1995]. The black arrows indicate the maximum cross-track (eastward) velocity anomalies at zero lag. The lags are negative when the transport lags the SLA.

onto the normalized transport time series (TT, BT and BC) at different lags (both negative and positive), and the statistical significance is tested using a two-sided Student *t* test. Note that 1 lag equals to 7 days as we are using weekly time series in this analysis.

Note that the BT- and BC-related SLA patterns line up in time without any time lag, as the TT-related SLA patterns (not shown) are nearly equal to the sum of the BT- and BC-related SLA patterns at the same lag.

4.1. Zero-Lag Regressions

The zero-lag SLA regressions onto the three transport time series (TT, BC, BT) are shown in Figure 8, with areas exceeding the significance level at 95% (dotted black lines) and 99% (solid black lines) being indicated. These regression maps illustrate the SLA patterns corresponding to one std of transport variability for each transport component. In all three cases, outstanding patterns appear along the Jason altimeter track #104 over which the transports have been calculated. However, in reality the track passes through the area of relatively weak sea level variability compared to either side of the track (see Figure 1b), suggesting that the along-track concentration of the strongest SLA patterns might be somewhat biased to project preferentially the transport variability in the vicinity of the track itself. Therefore, some caution is warranted when interpreting the results.

The most striking difference is observed between the BC (Figure 8b) and BT (Figure 8c) regressions, while the TT regressions (Figure 8a) reflect the mixed patterns of BC and BT, although TT better resembles BT than BC in the Yaghan Basin, but with an opposite tendency outside of the basin, as will be seen below. In the case of BC, the primary positive pole of SLA is found over the track immediately north of the SAF, south of which is a minor negative pole, which intensifies the SAF. The significant positive anomalies seen north of the SAF are not limited to the Yaghan Basin but extend far downstream all along the SAF tightly attached to the continental slope east of South America. There is also a significant correlation over the upstream continental slope along the west coast of South America. In addition, a secondary positive pole is found immediately north of the PF, strengthening the latter and forming a moderate SLA tripole along the track.

In great contrast to this, significant BT regressions are entirely confined within the Yaghan Basin, without any extension outside of the basin. They reveal a clear-cut intensified tripole along the track, but in phase opposition to that of BC, with a strong positive (negative) pole immediately south (north) of the SAF (PF). This corresponds to a situation where the SAF and the PF are approaching one of the other (the SAF extending southward and the PF northward), leading to a strong eastward velocity anomaly at 57°S (as marked by an arrow). The tripoles on the TT and BT regressions are quite similar in the Yaghan Basin (compare Figures 8a and 8c), the main difference being that the northern part of the TT tripole strengthens and extends far downstream along the continental slope in parallel with the SAF, a feature very similar to the case of BC (Figure 8b). It is worth recalling that a small transport at zero lag corresponds to SLA patterns with opposite signs to those of Figure 8, which corresponds in particular to a strong cyclone in the northern Yaghan Basin in the BT (or TT) regression map. This tripole pattern corresponds to strong positive deep (3000 m) transports between the SAF and PF jets (see Figure 7d). This is why the tripole is principally visible in TT and BT.

4.2. Lagged Regressions

In order to document the temporal evolution of the SLA field in the upstream and downstream of the Yaghan Basin in relation to the transport variability across the track, selected lagged regression maps of SLA onto the BC and BT transports are shown in Figures 9 and 10, respectively. These show quite different structures, with significant regressions (above the 95 or 99% confidence level) being observed over a wide range of lags for BC but only small lags around zero lag for BT.

Regression maps onto BC (Figure 9) give clear evidence of wave-train-like mesoscale SLA patches up to the far upstream area from DP, with a strong positive pole at the entrance to DP traveling eastward until it reaches the Phoenix Antarctic Ridge (PAR) at lag −23 week (about −5 months). It then slowly moves northward along the western side of the PAR where it stays while its amplitude grows. At lag −9 week (−2 months), the positive SLA pole begins to spread eastward along the continental slope, while its main part remains across the topography of the SFZ. At lag −2 week, the whole positive pole has passed over the topography and is located north of the SAF in the northern Yaghan Basin, while significant positive regressions are observed all around South America along the continental slope and on the WSR. At lag 0, a small negative pole appears over the track just south of the SAF, forming a tripole pattern to the north of the PF, as already mentioned. The tripole feature quite rapidly disintegrates at lag 2 week and no significant SLA signal is found along the track after lag 5-week (1 month).

Regression maps onto BT (Figure 10) show significant SLA patterns only after lag −7 week (less than −2 months), that is after the positive SLA associated with BC has entered the Yaghan Basin. The significant anomalies grow rapidly and remain confined to the central DP, in and on the sides of the Yaghan Basin. They are in phase opposition to the BC-associated SLA patterns (compare lag −2 week in Figures 9 and 10). The anomalies evolve rapidly, reach a maximum at lag 0 and then gradually dissipate on the topography surrounding the Yaghan Basin. A series of zoomed maps of BT regressions between lag −3 week to lag 5 week are shown in Figure 11, for the sake of clarity. For lags larger than 7 week (not shown), there is no significant pattern exceeding the 99% confidence level. In contrast to BC-related SLA patterns, most of significant BT-related SLA patterns are found only within the Yaghan Basin, without any connection to the upstream or downstream from the basin, regardless of lags. Moreover, the outstanding tripole pattern over the track is most clear from lag −2 week to lag 2 week, during which the eastward cross-track velocity anomalies in the region centered at 57°S are large, corresponding to a mature phase of the BT regressions.

4.3. Tentative Interpretations

The BC (and TT) regressed positive pole of SLA that builds up while it is blocked by the topography at the entrance to DP has been shown (Figure 9) to pass over the junction of the PAR and SFZ at lag −9 week (about −2 months). In terms of synoptic circulation, this positive SLA corresponds to a southward meander of the SAF at the entrance to DP, with its recurrent tendency close to annual periodicity, which can be seen

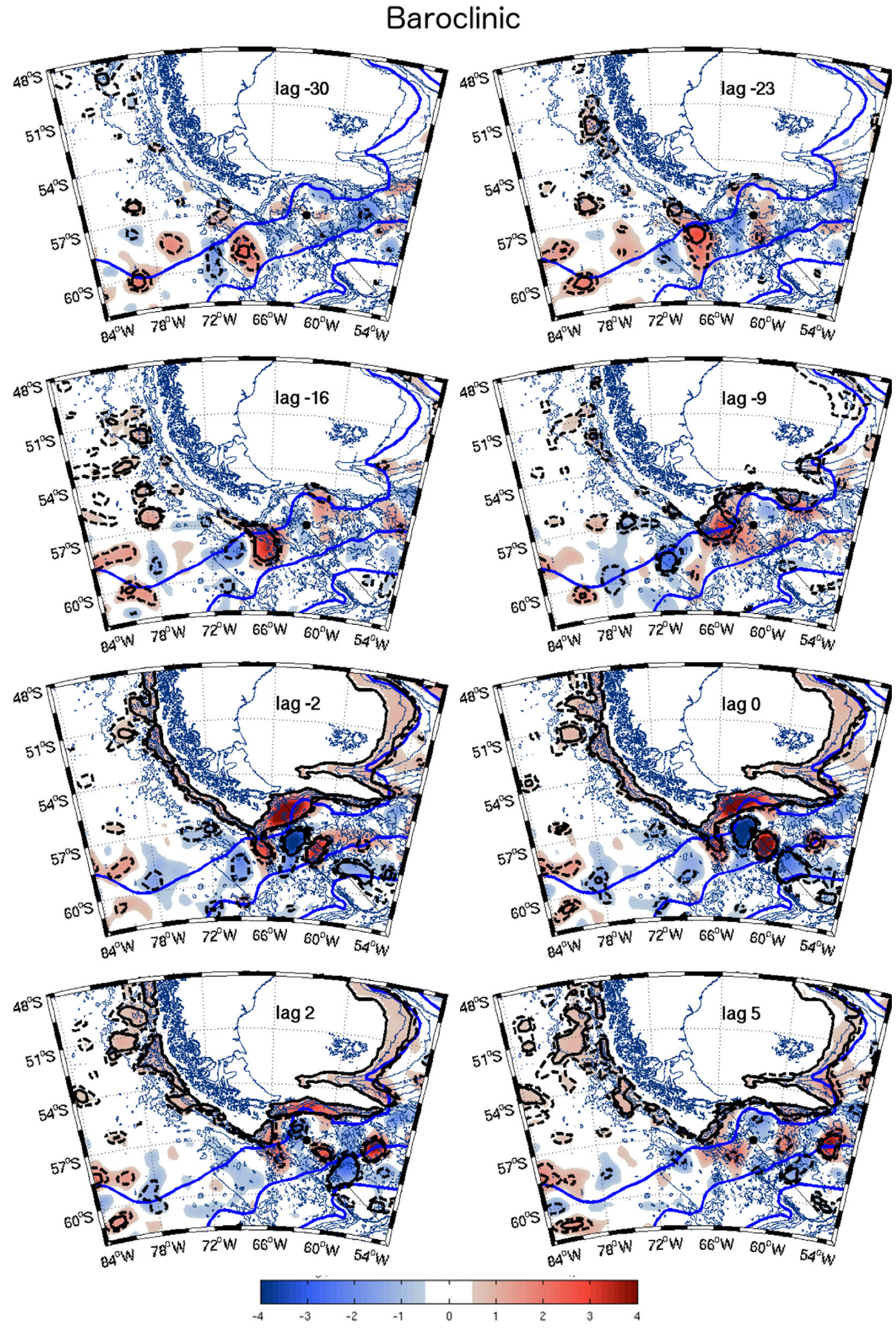

Figure 9. Same as Figure 8, except for lagged regressions at selected lags for the baroclinic transport component. The lags are negative when the transport lags the SLA.

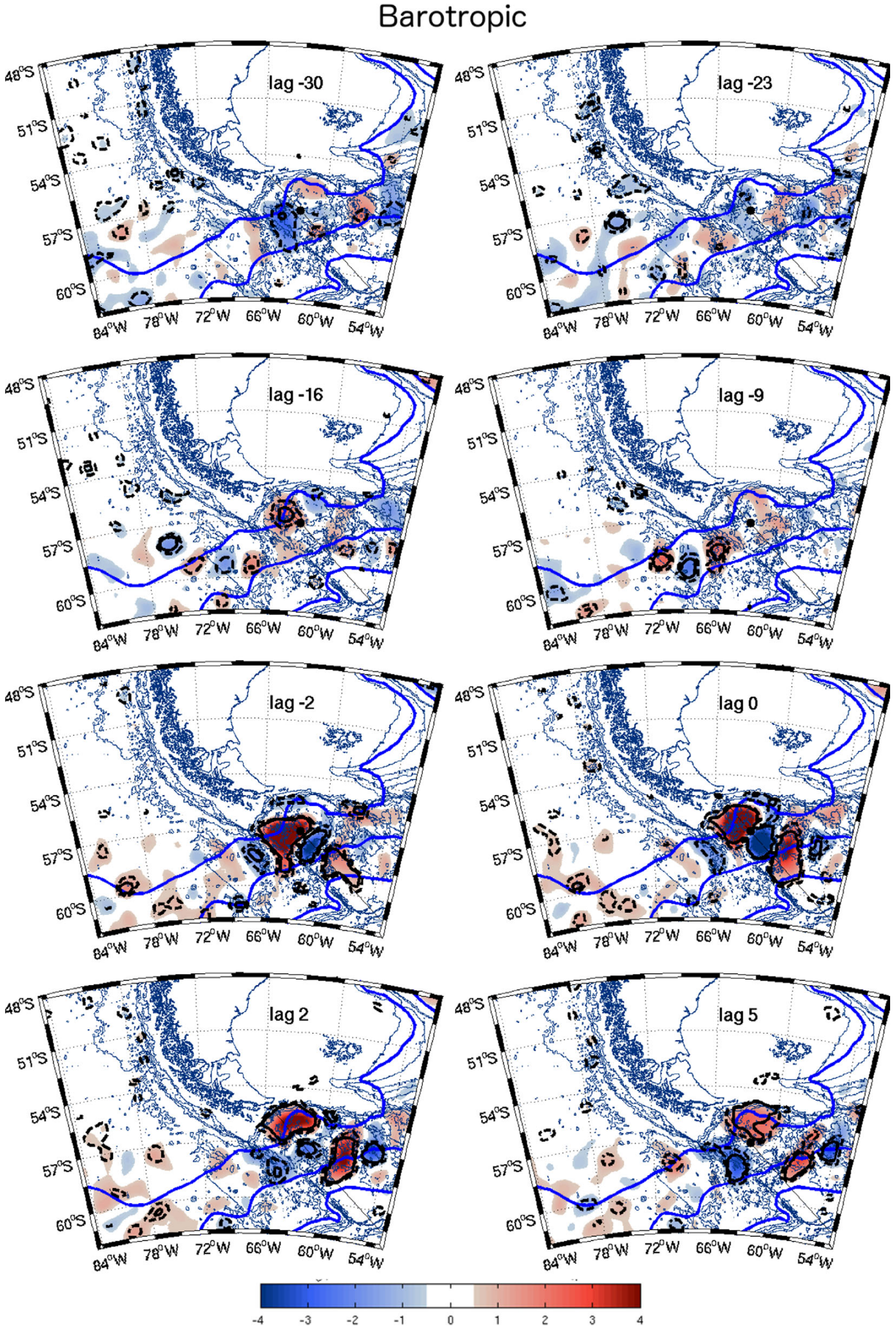

Figure 10. Same as Figure 8, except for lagged regressions at selected lags for the barotropic transport component. The lags are negative when the transport lags the SLA.

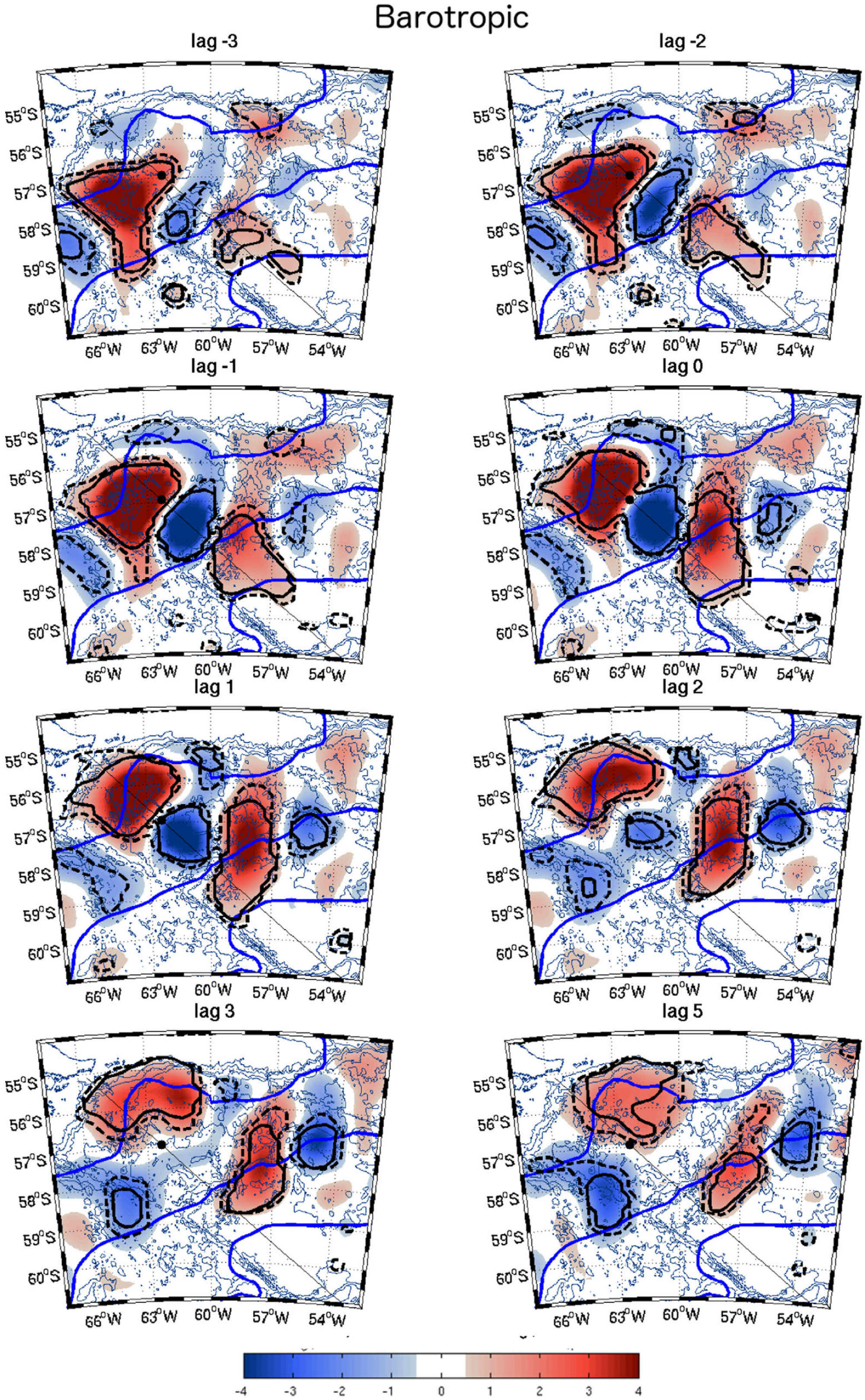

Figure 11. Same as Figure 10, except for zoomed regressions at selected lags between −3 and 5 weeks. The black dot is the point at 57°S on the Jason track 104. The lags are negative when the transport lags the SLA.

when comparing a series of regression maps of different lags (not shown). It then leaks over the SFZ before propagating around the Yaghan Basin following the continental slope and the northern slope of the WSR, creating a ring of positive anomalies on the edges of the Yaghan Basin and a depression in the center of the basin. The extremely rapid propagation speed of the order of a few m.s^{-1}, probably associated with coastal trapped waves, is not resolved in the 7 day apart altimetric SLA maps.

In contrast, the SLA patterns highly correlated with the BT are confined both in time (about 2 months) and space (in the Yaghan Basin and its periphery). This can be compared with the BC-regressed SLA patterns, which project much extensively both in time (over a year) and space (in the upstream area from DP and along the whole continental slope of South America). Therefore, the regression maps suggest at least three different timescales: an annual timescale for the meander blocked at the entrance to DP as observed in BC (or TT) regression maps; an intraseasonal timescale of about 50–70 days within the Yaghan Basin clearly observed in regression maps onto BT (or TT); and a weekly timescale for the BC (or TT) regressed SLA signal propagating along the continental slopes around South America.

The regression maps discussed above could suggest that the low-frequency positive SLA associated with BC at the entrance to DP, upon entering the Yaghan Basin, passing over the junction of the PAR and SFZ, triggers the intraseasonal SLA patterns highly correlated with BT as well as the BC-associated fast coastal trapped waves along the continental slope. While this may occur, correlation does not always imply causality and various sources can provoke barotropic variations and coastal trapped waves. Investigating coastal trapped waves and triggering of intraseasonal variability by the annual BC anomalies is a topic of future investigation outside the scope of this paper.

5. Potential Drivers of the Transport Variability

5.1. High-Frequency Intraseasonal Variability

We now test whether the observed spectral peaks at intraseasonal frequencies in the barotropic transport time series are consistent with classical barotropic basin modes. For this, we used here a formulation of the normal mode solution of stream function or barotropic basin modes in a rectangular basin given by *Longuet-Higgins* [1964] and *Weijer* [2008]. The details of the calculation are given in the Appendix A.

We obtain a phase speed $c = 6.3$ cm s^{-1} and a period $T = 100$ days for the lowest mode in the Yaghan Basin. The energy-conserving spectra of the transport time series (Figure 3) indicate that about 75% of the barotropic transport variability is confined within the intraseasonal band of periods shorter than 6 months. In the latter band, the barotropic component, which is the predominant contributor to the total variability compared to the partly compensating, minor variability from the baroclinic component, reveals five distinct peaks that are well correlated with the total variability at 28, 36, 50, 99, and 132 days (Figure 3). The peak at 99 days is very close to 100 days estimated from the basin mode formulation. We show in Appendix A that the observed westward phase speed is 6.9 cm s^{-1}, consistent to within 10% with the theoretical value of 6.3 cm s^{-1}. This suggests that the observed spectral peak centered at 99 days likely corresponds to the lowest basin mode of the Yaghan Basin. Note that higher modes are associated with much greater periods, so are irrelevant to intraseasonal variability.

However, the most energy-containing significant periods do not correspond to this basin mode but are rather at much smaller periods of 50, 36, and 28 days (Figure 3). These periods are close to 1/2, 1/3, and 1/4 of the observed basin mode period ($T = 99$ days), which likely correspond to "harmonics" having multiple products of the fundamental basin mode frequency. This implies that they might have resulted from the nonlinear interaction of flow such as that arising from the advective and bottom frictional terms in the momentum equation, which have not been taken into consideration in a linear vorticity dynamics in the basin mode formulation of *Longuet-Higgins* [1964]. These results strongly suggest that most intraseasonal transport variability in the Yaghan Basin, which acts otherwise as the predominant contributor to the DP transport variability, is associated not only with the barotropic basin mode centered at its fundamental period of 99 days but more energetically with its higher-frequency harmonics ($T = 50$, 36, 28 days) generated by strong nonlinear effects of the ACC within the Yaghan Basin.

How can more energetic harmonics compared to the fundamental basin mode be explained? One possibility for this may be via resonant amplification if the periods of harmonics are close to those of external forcing. Some hint for this appears in spectra of the Southern Annular Mode (SAM index; www.cpc.ncep.noaa.gov/products_precip/Cwlink/daily_ao_index/aao/aao.shtml) having salient energy peaks at 48 and 55 days (Figure 12a), very close to the 50 day harmonic. The 36 day harmonic is also close to a significant peak of local wind stress curl centered at 40 days (Figure 12b). The 28 day harmonic does not correspond to any peak in SAM nor in local wind stress curl but does correspond to the lunar monthly tide, Mn, which has a period of 27.55 days. In fact, the 28 day harmonic in BT and the Mn tidal component in the Yaghan Basin, which has been extracted from the Oregon State University global tide model TPXO62 [*Egbert and Erofeeva*, 2002] (www.esr.org/polar_tide_models/Model_TPXO62_load.html), are weakly but most significantly correlated each other at the zero lag ($r \sim -0.2$, significant at the 99% confidence level).

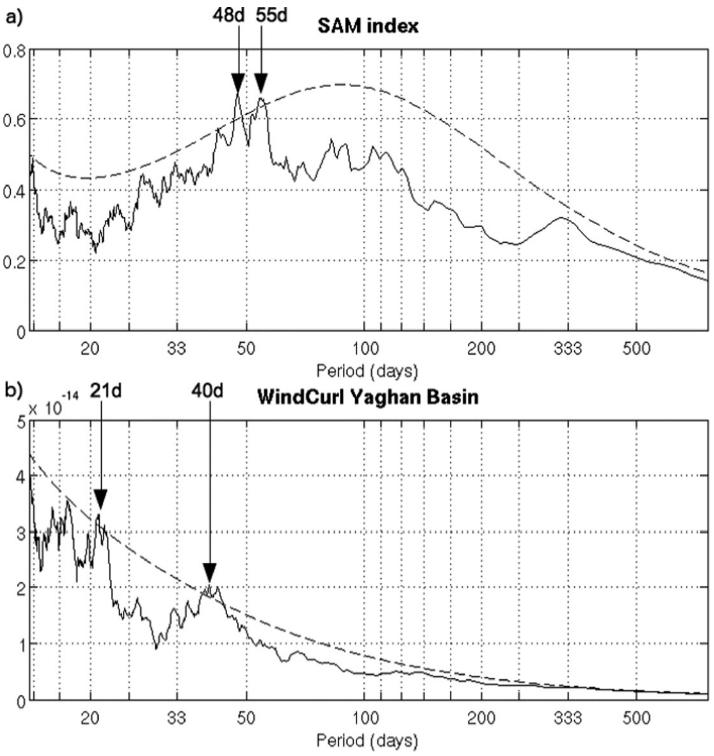

Figure 12. Variance-preserving spectra of (a) the weekly SAM index and (b) the local wind stress curl over the Yaghan Basin. The dotted lines show the 95% confidence level against the red noise background from an AR1 process.

Other processes can contribute to the intraseasonal SLA variations in the Yaghan Basin. For example, *Chereskin et al.* [2009] reported deep eddy generation between the SAF and PF with a timescale of about 2 months. From an 1 year array of 38 bottom moored Current and Pressure Recording Inverted Echo Sounders, these authors documented a spin up of strong deep eddies (up to 3000 m depth) associated with meanders of the surface fronts in the Yaghan Basin. The 50 day barotropic and baroclinic signals are significantly anticorrelated at lag 0 ($r = -0.46$), with decreasing correlation with lags. The deep eddy generation mechanism may thus explain at least partially the 50 day BT spectral peak.

5.2. Low-Frequency Transport Variability Due to SAM and ENSO

We seek potential drivers of the observed low-frequency variations in total transport and perform a coherence analysis of the 5 week smoothed total transport with large-scale climate indices (SAM, Nino 3.4) previously shown to potentially influence transport variations [*Close and Naveira Garabato*, 2012]. The weekly-averaged normalized and detrended SAM index time series (1993–2013) has significant energy (above the 95% confidence level) at the annual period at the beginning of the time series until 2000 and then at the biannual period from 2000 to 2012. A 5 year variability is present all along the time series, particularly until 2006, although it is not significant due to the limited data length. The weekly-averaged normalized Nino 3.4 Index time series (from http://www.cpc.ncep.noaa.gov/data/indices/wksst8110.for) over 1993–2003 displays two significant peaks of energy, one at the typical 4–5 years period, the other around 1.5–2 years (not shown). A wavelet coherence analysis (not shown) indicates that the two indices bear no relation to each other except at the annual period at the end of the time series (2007–2013) when they are significantly anticorrelated.

The total transport is strongly correlated ($r > 0.8$) and in phase with the SAM index at an approximately annual period near the beginning of the time series (from 1994 to 1999), and an approximately biannual period after 2006 (Figure 13a). The shift from annual to biannual correlation corresponds to the shift in SAM index periodicity mentioned above. There is no coherence between the transport and SAM from 1999 to 2006. The total transport is also significantly correlated with the ENSO index at the annual to biannual period from 2000 to 2004 (Figure 13b), at a time when the total transport shows no coherence with SAM (Figure 13a). The

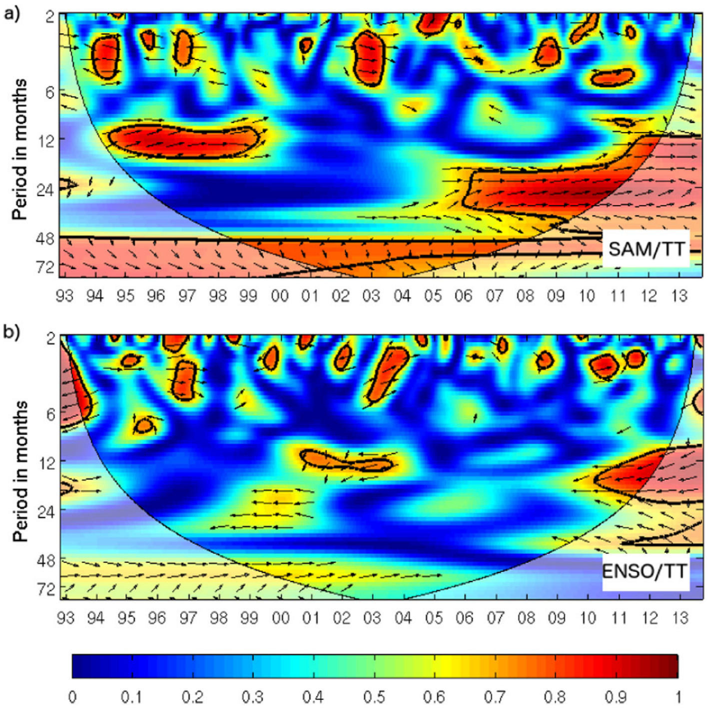

Figure 13. Wavelet coherence between the total transport and (a) the SAM index and (b) the Nino 3.4 index. Time series have all been filtered with a one month low-pass filter. The correlation is shown in color and the phase lag in arrows turning clockwise from due east (zero lag). Black lines indicate the 95% confidence level. Faint colors outside of the contours correspond to statistically insignificant areas.

coherence becomes significant at the annual period but with an opposite phase from 2009 to 2013. The lag between the ENSO index and total transport varies between 6 months and a year (Figure 13b).

The wavelet coherence analysis suggests that the total transport is successively influenced by SAM (1993–1999), then by ENSO (2000–2004), and finally by a combination ENSO+SAM (2006–2013) when the two climate indices are significantly anticorrelated at the annual period. The correlation with the ENSO index appears 6 months to 1 year after the 1998 strong El Niño event followed by strong La Niña events until 2001, a time when the SAM index is of rather small amplitude (not shown). In summary, there appears no systematic consistent response to low-frequency forcing by SAM or ENSO, but their respective influences are intermittent and epoch-dependent, aside from very low spectral energy contained in nonseasonal low frequencies, especially for periods greater than 2 years. Further analysis with much longer transport time series is needed.

6. Summary and Discussion

Detailed statistical analyses of the transport variability across DP have been performed from the 20 year long time series of volume transport referenced to 3000 m previously prepared by *Koenig et al.* [2014] using the combined data sets of satellite altimetry and direct current measurements along the Jason altimeter track 104 during the recent DRAKE project [*Provost et al.*, 2011]. We also produced transport time series referenced to the bottom in *Koenig et al.* [2014] by extrapolating the look-up table from 3000 m to the bottom. The analysis of the transport time series referenced to the bottom yielded very similar results and conclusions.

The along-track distribution of the mean total transport shows large eastward transports near the four major fronts (SAF, PF, SACCF-N, SACCF-S) and a westward transport in a region centered at 57°S between the SAF and PF in the Yaghan Basin and at 59.7°S between the SACCF-N and SACCF-S in the Ona Basin (Figure 5). The region centered at 57°S appears as a strategic point for DP transport monitoring as the whole-track TT is highly correlated with local TT ($r = 0.53$) and BT ($r = 0.69$) around 57°S. In contrast, the local transport variability in the center of the Ona Basin does not contribute significantly to the whole-track variability. Moreover, most of BC variability is confined in the Yaghan Basin, with a negligible contribution from the Ona Basin (Figure 5b). Therefore, the transport variability in these two basins appears to occur nearly independently and the whole-track TT is preferentially controlled by transports in the Yaghan Basin, especially by BT of the region centered at 57°S.

While the time-mean whole-track TT (140 Sv) is largely determined by the BC component (112 Sv), with a minor contribution from the BT component (28 Sv), its temporal variability shows the opposite tendency. In fact, the strongest transport variability is associated with BT (12 Sv std) and the least variability with BC (7 Sv std), with the TT variability (10 Sv std) lying in between the two, indicating that the BC variability is partly compensating the BT variability, consistent with a significant anticorrelation ($r=-0.5$) between the BT and BC variability.

In terms of the frequency content, the intraseasonal variability of periods of 1–5 months constitutes the majority of the variability for all three transport components (Figure 3). Common to both BT and TT are two energy-containing frequency bands, one for periods of 1–2 months and the other for 3–5 months. These contain significant peaks centered at 28, 36, and 50 days in the 1–2 month band and distinctive (though not significant at the 95% level) peaks at 99 and 132 days in the 3–5 month band. Among these, the 36 day and 50 day peaks constitute the most energetic signals. The spectral energy decreases sharply with increasing periods with significant low-frequency signals only at annual and biannual timescales.

The lagged SLA regressions onto the three transport components reveal different projections in space and time according to each component (Figures 8–11). It is found that the SLA patterns significantly correlated with BT are confined entirely within the Yaghan Basin, with a representative intraseasonal timescale of about 2 months. This is consistent with the observations by *Chereskin et al.* [2009]. In contrast, the BC-regressed SLA patterns project much more extensively in the upstream area from DP as slowly propagating wave-trains annually recurrent at the entrance to DP on one hand, and on the other hand, along the whole continental slope of South America as quickly propagating coastal trapped waves-like features. The TT-regressed SLA patterns are very similar to those of the BT (BC) regressions inside (outside) the Yaghan Basin. At zero lag, there appear well-defined SLA tripoles along the track (Figure 8), with the BT (and TT) tripole being in phase opposition to the BC tripole. The BT/TT tripole can be nicely employed for depicting the meandering SAF associated with TT extrema (Figure 7), with TT maxima being matched with an anomalous anticyclone (cyclone) just south (north) of the mean SAF (PF), inducing a southward meandering of the synoptic SAF, and vice versa for TT minima.

All above results indicate that the intraseasonal BT variability (in the upper 3000 m) in the Yaghan Basin is not generated and advected from the exterior rather is developed within the Yaghan Basin where it eventually dissipates without propagating outside of the basin. In other words, it should be a unique feature to the basin, i.e., a basin mode. Testing the classic barotropic basin mode model of *Longuet-Higgins* [1964] with parameters appropriate for the Yaghan Basin (Appendix A) led to mixed results. The model explains the BT/TT spectral peak centered at 99 days well, and the associated westward phase speed error is within 10%. However, the model does not explain the major significant peaks, especially the most outstanding peaks at 36 and 50 days, suggesting other mechanism(s). We have speculated whether the nonlinear effects of the powerful ACC in the basin generate multiple harmonics of the fundamental basin mode, which could then be resonantly amplified with the SAM forcing and local wind stress curl having significant spectral peaks around 50 and 40 days, respectively (Figure 12). More work is needed to get a deeper insight of the generating mechanism of these intraseasonal BT signals, which is currently underway by analyzing the outputs of an eddy-resolving global ocean model (courtesy of G. Garric, Mercator Ocean, Toulouse, France).

Finally, we would like to briefly mention that aside from moderate annual to biannual signals, the interannual transport variability at DP is found to be completely overwhelmed by prevalent intraseasonal variability, at least during the last two decades we examined here. Moreover, we have not found any systematic relationship between climatic indices such as SAM or ENSO and the DP transport variability, but their covariability depends on a particular epoch and periodicity in question (Figure 13). Also, the relatively short data length (20 years) inhibits us from documenting any decadal-scale variability of the DP transport and its response to concomitant atmospheric forcing. Much longer transport data are needed to address these questions.

Appendix A: Barotropic Basin Modes

From an array of current meters deployed in the southern Mascarene Basin, *Warren et al.* [2002] discovered a resonance-excited Rossby basin mode with a bimonthly period (59 days). This is supported by *Weijer* [2008] who analyzed the normal modes of the Mascarene Basin using a barotropic shallow-water model and showed the existence of several modes with periods between 40 and 70 days that are consistent with the observations. Based on a similar model, *Weijer et al.* [2007] also found multiple oscillatory modes of the Argentine Basin. The theoretical development of the latter modes in a rectangular enclosed basin is given

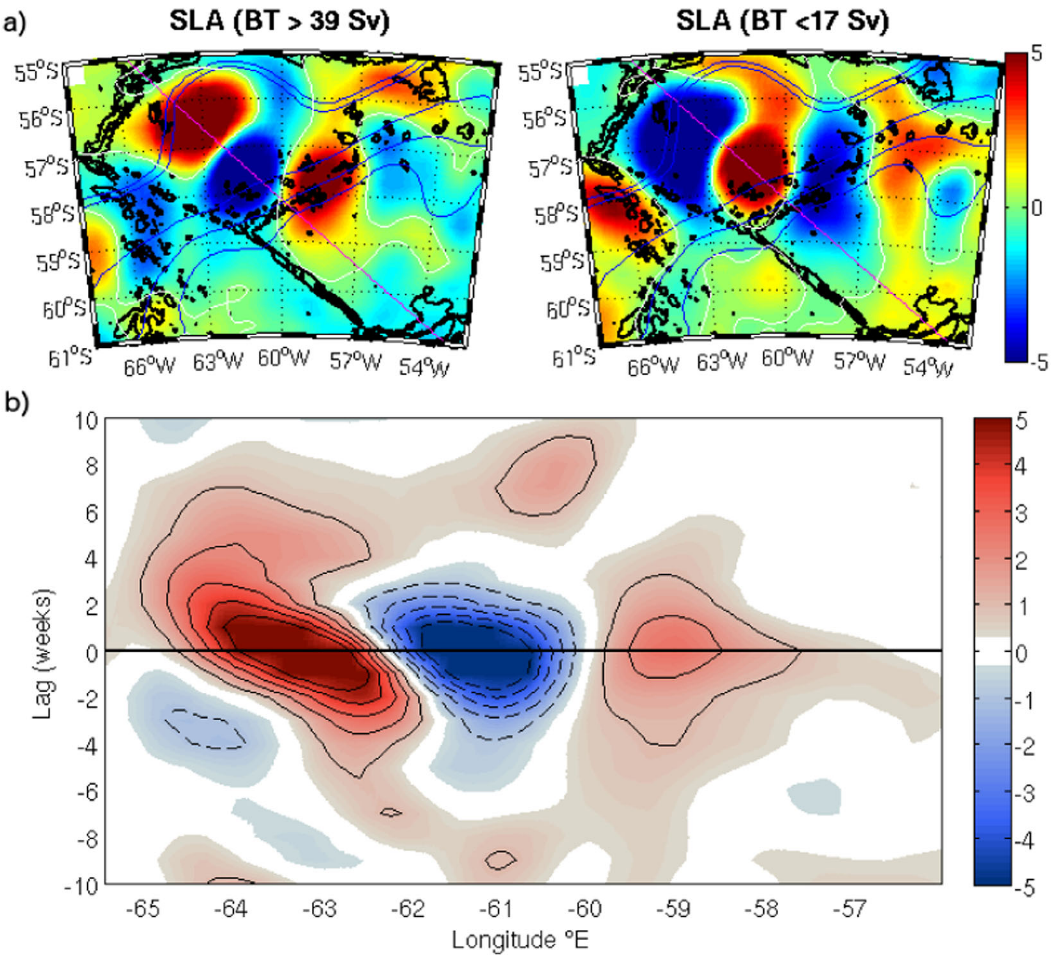

Figure A1. (a) SLA composite map corresponding to the barotropic transport (a) greater than 39 Sv (or one std greater than the mean BT) and smaller than 17 Sv (or one std smaller than the mean BT). The magenta line is the Jason track #104. Color scale is in centimeter. The red lines are the actual position of the fronts (two branches of the SAF, two branches of the PF and SACCF-N). The blue lines indicate the time-mean position of the fronts over 20 years of altimetric data. Bathymetry is shown in bold black lines. (b) Lagged SLA regressions onto the barotropic transport along the Jason track 104. The lags are in week and a negative (positive) lag means SLA leads (lags) the transport time series.

in *Longuet-Higgins* [1964], while a practical application of the method in the Mascarene Basin by *Weijer* [2008] is particularly instructive.

The normal mode solution of stream function for barotropic basin modes (m, n) in a rectangular basin of (zonal x meridional) dimensions $a \times b$ is given as [*Longuet-Higgins*, 1964; *Weijer* 2008]:

$$\psi = \sin\left(\frac{m\pi x}{a}\right)\sin\left(\frac{n\pi y}{b}\right)e^{-i(\gamma_{mn}x+\sigma_{mn}t)} \quad \text{with } m\,(\text{or } n)=1,\ 2,\ 3\ \ldots, \tag{1}$$

$$\gamma_{mn} = \sqrt{\left(\frac{m\pi}{a}\right)^2 + \left(\frac{n\pi}{b}\right)^2}, \tag{2}$$

$$\sigma_{mn} = \frac{\beta}{2\gamma_{mn}}, \tag{3}$$

where $\beta = \partial f/\partial y$ is the meridional gradient of the Coriolis factor, $f = 2\varpi \sin(\phi)$, ϖ ($\sim$7.292 $\times 10^{-5}$ s^{-1}) is the angular velocity of the Earth's rotation, and ϕ is the latitude.

The double sine functions of (1) represent the spatial amplitudes of the normal modes satisfying the no normal flow condition at the basin boundaries ($x = 0$, a; $y = 0$, b) and $e^{-i(\gamma_{mn}x+\sigma_{mn}t)}$ is the carrier wave propagating westward with a phase speed c and a period T, which are, using the dispersion relationship (3):

$$c=\frac{-\sigma_{mn}}{\gamma_{mn}}=\frac{-2\sigma_{mn}^2}{\beta}=\frac{-\beta}{2\gamma_{mn}^2}, \tag{4}$$

$$T=\frac{2\pi}{\sigma_{mn}}=\frac{4\pi\gamma_{mn}}{\beta}. \tag{5}$$

Taking $a=700$ km, $b=350$ km, and $\beta=1.263\times10^{-11}$ m^{-1} s^{-1} at 56.5°S for the Yaghan Basin, we obtain $c=6.3$ cm s^{-1} and $T=100$ days for the lowest mode ($m=n=1$), according to (4) and (5).

In order to analyze the westward propagation of the basin mode, we show in Figure A1b the lagged regressions of SLA on track 104 onto the barotropic transport time series. Significant regressions are confined within the Yaghan Basin between 60° and 65°W and within ± 2 lags (±14 days), with the strongest westward phase speed of 6.2 cm s^{-1} being observed in the region between 62° and 64.5°W (Figure A1b). This phase speed is calculated along the altimetric track that is inclined about 45° westward from due north, so it does not represent the real westward speed. To estimate correctly the latter speed, we need the information about the tilt that the SLA field (as a proxy of the stream function) forms relative to the *x*-*y* coordinates. The composite maps of SLA corresponding to barotropic transport extrema (Figure A1a) hint at an overall tilt of about 30° eastward from due north, roughly parallel with the SW-NE-oriented northwestern side of the Yaghan Basin. Taking into account this tilt, we have obtained finally the westward phase speed of 6.9 cm s^{-1}, which is about 10% greater than that from the basin mode analysis (6.3 cm s^{-1}).

The agreement between these theoretical and observational characteristics of the basin mode is striking, considering the approximations made for the rectangular basin from the rather irregularly shaped complex Yaghan Basin as well as the rough estimation of the orientation of the SLA field.

Acknowledgments

This paper is a contribution to the DRAKE project that was funded both by CNES (Centre National d'Etudes Spatiales) through the OST/ST altimetric program and by CNRS-INSU (Institut des Sciences de l'Univers) through the LEFE program. We thank Peter Sutherland for most valuable comments on the manuscript and Young-Oh Kwon at WHOI who kindly communicated the code calculating the significance level of spectra against the AR1 red noise model. The current meter data are available at LOCEAN (Christine Provost: cp@locean-ipsl.upmc.fr) and the altimetry data at AVISO (CLS Argos; http://www.aviso.altimetry.fr/en/data.html).

References

Barré, N., C. Provost, N. Sennéchael, and J.H. Lee (2008), Circulation in the Ona Basin, southern Drake Passage, *J. Geophys. Res.*, *113*, C04033, doi:10.1029/2007JC004549.

Barré, N., C. Provost, A. Renault, and N. Sennéchael (2011), Mesoscale activity in Drake Passage during the cruise survey ANT-XXIII/3: A satellite perspective, *Deep Sea Res., Part II*, *58*(25), 2533–2554, doi:10.1016/j.dsr2.2011.01.003.

Barriopedro, D., R. García-Herrera, and R. M. Trigo (2010), Application of blocking diagnosis methods to general circulation models. Part I: A novel detection scheme, *Clim. Dyn.*, *35*(7–8), 1373–1391.

Chereskin, T., K. Donohue, D. Watts, K. Tracey, Y. Firing, and A. Cutting (2009), Strong bottom currents and cyclogenesis in Drake Passage, *Geophy. Res. Lett.*, *36*, L23602, doi:10.1029/2009GL040940.

Chidichimo M. P., K. A. Donohue, D. R. Watts, and K. L. Tracey (2014), Baroclinic Transport time series of the Antarctic circumpolar current measured in Drake Passage, *J. Phys. Oceanogr.*, *44*, 1829–1853.doi:10.1175/JPO-D-13-071.1

Close, S. E., and A. C. Naveira Garabato, (2012), Baroclinic adjustment in Drake Passage driven by tropical Pacific forcing, *Geophy. Res. Lett.*, *39*, L19610, doi:10.1029/2012GL053402.

Cunningham, S., S. Alderson, B. King, and M. Brandon (2003), Transport and variability of the Antarctic Circumpolar Current in Drake Passage, *J. Geophy. Res.*, *108*(C5), 8084, doi:10.1029/2001JC001147.

Egbert, G. D., and S. Y. Erofeeva (2002), Efficient inverse modeling of barotropic ocean tides, *J. Atmos. Oceanic Technol.*, *19*(2), 183–204.

Ferrari, R., C. Provost, A. Renault, N. Sennéchael, N. Barré, Y.-H. Park, and J. Lee (2012), Circulation in Drake Passage revisited using new current time series and satellite altimetry: 1. The Yaghan Basin, *J. Geophy. Res.*, *117*, C12024, doi:10.1029/2012JC008264.

Ferrari, R., C. Provost, N. Sennéchael, and J. Lee (2013), Circulation in Drake Passage revisited using new current time series and satellite altimetry: 2. The Ona Basin, *J. Geophy. Res.*, *118*, 147–165, doi:10.1002/2012JC008193.

Hallberg, R., and A. Gnanadesikan (2006), The role of eddies in determining the structure and response of the wind-driven Southern Hemisphere overturning: Results from the Modeling Eddies in the Southern Ocean (MESO) project, *J. Phys. Oceanogr.*, *36*, 2232–2252.

Hughes, C. W., P. L. Woodworth, M. P. Meredith, V. Stepanov, T. Whitworth and A. R. Pyne (2003), Coherence of Antarctic sea levels, Southern Hemisphere annular mode, and flow through Drake Passage, *Geophys. Res. Lett.*, *30*(9), 1464, doi:10.1029/2003GL017240.

Koenig Z., C. Provost, R. Ferrari, N. Sennéchael and M.-H. Rio (2014), Volume transport of the Antarctic Circumpolar Current: Production and validation of a 20 year long times series obtained from in situ and satellite data, *J. Geophys. Res. Oceans*, *119*, 5407–5433, doi:10.1002/2014JC009966.

Longuet-Higgins, M. S. (1964), Planetary waves on a rotating sphere, *Proc. R. Soc. London Ser. A*, *279*(1379), 446–473.

Meredith, M., and A. M. Hogg (2006), Circumpolar response of southern ocean eddy activity to a change in the southern annular mode, *Geophy. Res. Lett.*, *33*, L16608, doi:10.1029/2006GL026499.

Meredith, M. P., P. L. Woodworth, C. W. Hughes and V. Stepanov (2004), Changes in the ocean transport through Drake Passage during the 1980s and 1990s, forced by changes in the Southern Annular Mode, *Geophys. Res. Lett.*, *31*, L21305, doi:10.1029/2004GL021169.

Meredith, M. P., et al. (2011), Sustained monitoring of the southern ocean at drake passage: Past achievements and future priorities, *Rev. Geophys.*, *49*, RG4005, doi:10.1029/2010RG000348.

North, G. R., T. L. Bell, R. F. Cahalan and F. J. Moeng (1982), Sampling errors in the estimation of empirical orthogonal functions, *Mon. Weather Rev.*, *110*(7), 699–706.

Nowlin, J. W., T. Whitworth, and R. Pillsbury (1977), Structure and transport of the Antarctic circumpolar current at Drake passage from short-term measurements, *J. Phys. Oceanogr.*, *7*, 778–802.

Orsi, A. H., I. T. Whitworth, and J. W. Nowlin (1995), On the meridional extent and fronts of the Antarctic circumpolar current, *Deep Sea Res., Part I*, *42*, 641–673.

Provost, C., A. Renault, N. Barré, N. Sennéchael, V. Garçon, J. Sudre, and O. Huhn (2011), Two repeat crossings of Drake passage in austral summer 2006: Short-term variations and evidence for considerable ventilation of intermediate and deep waters, *Deep Sea Res., Part II*, *58*(25–26), 2555–2571, doi:10.1016/j.dsr2.2011.06.009.

Renault A., C. Provost, N. Sennéchael, N. Barré, and A. Kartavsteff (2011), Two full-depth velocity sections in the Drake Passage in 2006: Transport estimates, *Deep Sea Res., Part II*, *58*(25), 2572–2591, doi:10.1016/j.dsr2.011.06.009.

Thompson, D. W. and S. Solomon (2002), Interpretation of recent Southern Hemisphere climate change, *Science*, *296*(5569), 895–899.

Warren, B. A., T. Whitworth, and J. H. LaCasce (2002), Forced resonant undulation in the deep Mascarene Basin, *Deep Sea Res., Part II*, *49*(7), 1513–1526.

Weijer, W. (2008), Normal modes of the Mascarene Basin, *Deep Sea Res., Part I*, *55*(1), 128–136, doi:10.1016/j.dsr.2007.10.005.

Weijer, W., F. Vivier, S. T. Gille, and H. A. Dijkstra (2007), Multiple oscillatory modes of the Argentine Basin. Part II: The spectral origin of basin modes. *J. Phys. Oceanogr.*, *37*(12), 2869–2881, doi:10.1175/2007JPO3688.1.

Whitworth, T. (1983), Monitoring the transport of the Antarctic circumpolar current at Drake Passage, *J. Phys. Oceanogr.*, *13*, 2045–2057.

Whitworth, T., and R. Peterson (1985), Volume transport of the Antarctic Circumpolar Current from bottom pressure measurements, *J. Phys. Oceanogr.*, *15*, 810–816.